Modeling the Effect of Microstructural Variability on Solder Joint Lifetime

AE5711 Thesis Aerospace Structures & Materials

Delft University of Technology
NXP Semiconductors
Matteo Rebosolan

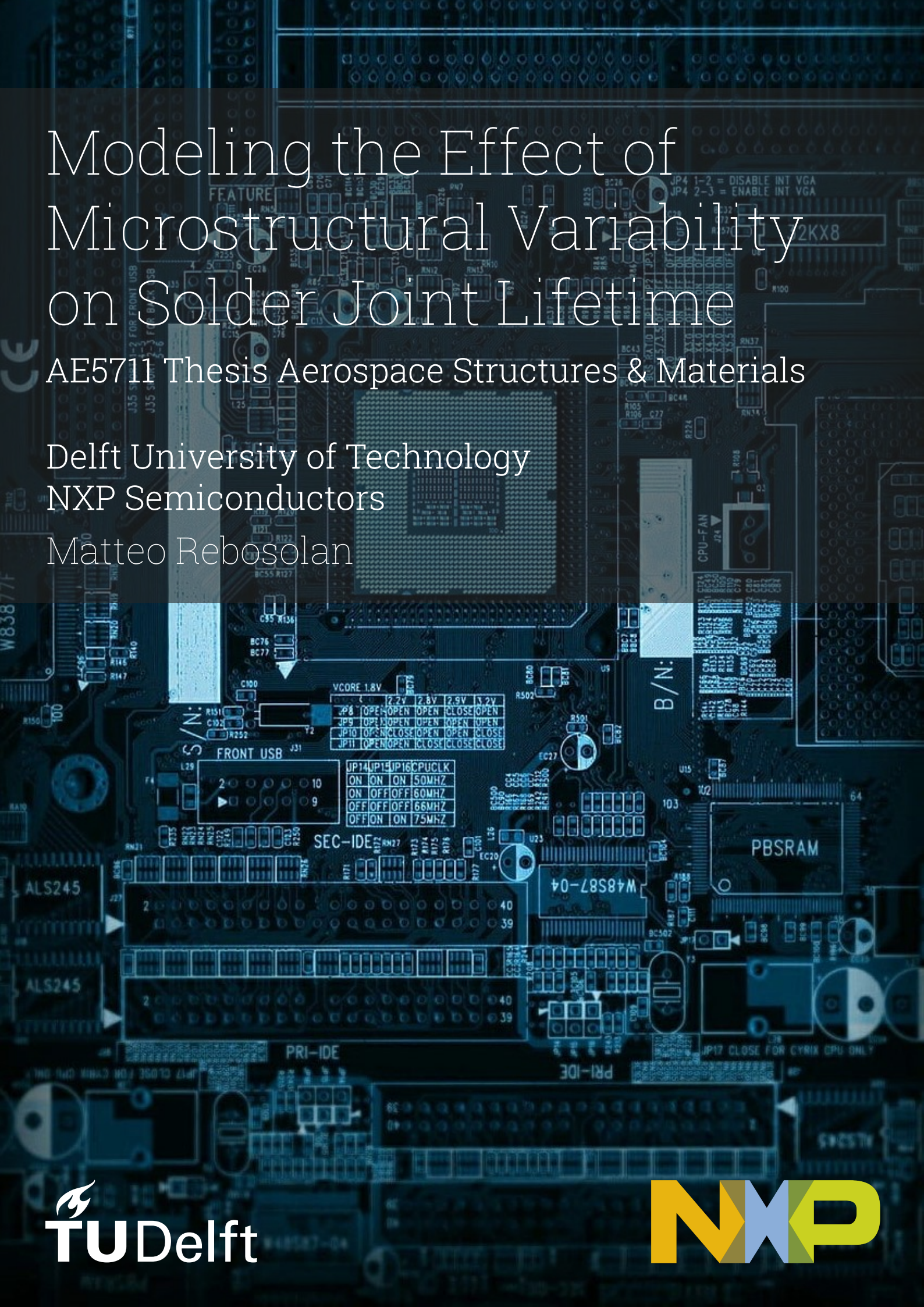

TU Delft

NXP

Modeling the Effect of Microstructural Variability on Solder Joint Lifetime

AE5711 Thesis Aerospace Structures & Materials

by

Matteo Rebosolan

to obtain the degree of Master of Science
at the Delft University of Technology,
to be defended publicly on June 15th, 2023

Student Name	Student Number
Matteo Rebosolan	4664973

University Supervisor:	Dr. Boyang Chen
Company Supervisor:	Dr.ir. Michiel van Soestbergen
Project Duration:	July, 2022 - May, 2023
Faculty:	Faculty of Aerospace Engineering, Delft

TU Delft NXP

Preface

This thesis is the icing on the cake of a six-year experience that made me into an almost unrecognizable person from the small town kid that first set foot in the Netherlands at 18. While I treasure the technical knowledge I acquired over the years, the most important lessons TU Delft taught me have to do with character. I learned that nothing worth having comes easy, but it also taught me that hard work and passion are always rewarded.

No man is completely self-made. I would not have got to this point without the help of multiple amazing people that encouraged me to push my limits and were ready to support me when the going got tough, be it during my thesis or in the academic career that came before it. I would like to thank NXP Semiconductors for giving me the opportunity to work on such an exciting topic for my thesis and for jump-starting my professional career. I am extremely grateful to dr.ir. Michiel van Soestbergen and dr. Boyang Chen for their exemplary supervision. They were present along every step of the way and enabled me to see this thesis to the end. I would also like to thank dr.ir. Jeroen Zaal for the valuable technical and not-so-technical discussions.

My time in Delft and Nijmegen would not have been so memorable without all the friends I made along the way, in particular Lukas, Mohammad, Arudra and Youssef. I am thankful for the many adventures we had together and for those yet to come. A BIG thank you to my parents, Michele & Roberta for supporting my ambitions and for shaping me into the man I am today and to my brother Marco for being my partner in crime. Special thanks to my uncle Davide for generously sharing his immense wealth of knowledge on every subject known to mankind with me (if you know you know). Last but not least, I want to thank my girlfriend Zeynep for being there for me every single day and for making my life so much more fun by being the goofy counterpart to my seriousness.

I hope you enjoy reading this thesis just as much as I enjoyed working on it.

Matteo Rebosolan
Delft & Nijmegen, June 2023

Contents

Abstract

The objective of this thesis was to develop a microstructure-based FE modeling technique to be used in solder joints for semiconductor packaging applications. This technique is capable of generating random solder joint microstructures featuring $\beta - Sn$ grains and grain boundaries by means of 3D Voronoi tessellations. The anisotropic material behavior of $\beta - Sn$ grains is described by the Garofalo-Hill creep model, which combines the Garofalo creep equation with the anisotropic Hill equivalent stress definition . The $\beta - Sn$ grains also feature anisotropic elastic behavior. The grain boundaries are implemented in the FE models as interface elements and they are fitted with a custom-developed constitutive model. This constitutive model combines isotropic creep and isotropic elasticity. The granular microstructure of SAC solder joints is generated via random Voronoi tessellations. The tessellations are used to automatically generate large amounts of unique solder joints with 5 to 9 grains each, with each grain having a random material orientation.

The modeling technique was used to qualitatively estimate the stochastic variability that the microstructural differences introduce in the creep response of the solder joints. Multiple simulation campaigns were performed to analyze this variability on a single solder joint level as well as on a product level. A number of sample products with random combinations of unique solder joints were developed for the latter campaign.

According to methods in the literature, the volume-averaged creep strain energy density was correlated with fatigue failure in order to estimate the microstructure-induced stochastic variability. The grains with the highest creep strain energy density were treated as the most critical with respect to failure. On a single solder joint level, a lifetime variability of a factor of 4.1 was observed. On a product level, this reduced to a factor of 2.6. The statistical distributions resulting from the simulations were also compared with real-life reliability data.

List of Figures

List of Tables

Nomenclature

Abbreviations

Abbreviation	Definition
ATC	Accelerated Thermal Cycling
BCT	Body-Centered Tetragonal
BGA	Ball Grid Array
CALCE	Center for Advanced Lifecycle Engineering
CS	Coordinate System
CSED	Creep Strain Energy Density
CSR	Creep Strain Rate
CTE	Coefficient of Thermal Expansion
FE(M)	Finite Element (Modeling)
IC	Integrated Circuit
IMC	InterMetallic Compound
IML	InterMetallic Layer
LOR	Level Of Refinement
PCB	Printed Circuit Board
PLM	Polarized Light Microscopy
QFN	Quad Flat-No Leads
SAC	SnAgCu Alloy
WLCSP	Wafer-Level Chip-Scale Package

Symbols

Abbreviation	Definition
α	Weibull characteristic life
β	Weibull shape parameter
Δt	Time step
$\dot{\epsilon}^{cr}$	Creep strain rate
$\dot{\epsilon}^{cr}_{Hill}$	Equivalent Hill creep strain rate
$\dot{\epsilon}^{cr}_{ij}$	Creep strain rate tensor
$\dot{\epsilon}^{el}$	Elastic strain rate
$\dot{\epsilon}_{tot}$	Total strain rate
ν	Poisson's ratio
σ_{eq}	Equivalent stress
σ_{Hill}	Hill stress
σ_{ij}	stress tensor
σ_n	Normal stress
σ_{vm}	von Mises stress
τ_1, τ_2	In-plane shear stresses
A_{GB}	Grain boundary creep constant
C_1, C_2, C_3, C_4	Garofalo creep model constants
D	Stiffness matrix
E	Young's modulus
F, G, H, L, M, N	Hill anisotropy constants
N_f	Number of cycles to failure
R_y	Rotation matrix around y-axis
t_{cz}	Constitutive thickness
T	Temperature
u_{ij}	Displacement vector
$\dot{u}^{cr}$	Creep displacement rate
$\dot{u}_{GB}$	Grain boundary displacement rate
superscript ^{i}	Value at increment i
superscript $^{i+1}$	Value at increment $i+1$

1

Introduction

The semiconductor industry has been at the forefront of technological innovation for decades. Electronic devices are a cornerstone of our modern lifestyle and almost all of them function by means of semiconductors. The breadth and relevance of this industry on society is reflected in the amount of attention it garners in the world of geopolitics: all the major powers such as the United States, Europe, China and India are devoting significant effort to protecting and expanding their semiconductor ecosystems, from design to production and application.

Semiconductor companies are not only focused on improving the performance of their products but their robustness and reliability as well. New and upcoming technologies such as driverless automotive impose extremely stringent safety requirements, as electronic malfunctions could be catastrophic. Ensuring product reliability has become crucial for industry players. NXP Semiconductors' "Total Quality" philosophy is a testament to this:

> *"Total Quality drives us to make the connected world better, safer and more secure. When customers think of NXP, we want them to think Total Quality — first-time-right development, designs and qualification; zero defects delivered to our customers; and flawless customer support"*.

In order to function, semiconductors need to be enveloped in a so-called "package". Packages allow the semiconductor's integrated circuit (the "core" of the whole assembly) to communicate with the environment while at the same time protecting it from the environment itself [1]. The package is usually connected to a Printed Circuit Board (PCB) by minuscule solder joints. The repeated high temperatures and high power densities generated by the integrated circuit throughout its operational lifetime give rise to mechanical issues in the package, such as warpage of the package and delamination of interfaces [2] [3]. The package, the integrated circuit and the PCB have different coefficients of thermal expansion

(CTE): they will therefore contract and shrink at different rates, causing cyclical stresses and fatigue in the solder joints that act as connectors [4]. This makes solder joints critical for the reliability of the whole device: a single solder joint failure can cause failure of the whole semiconductor device [4]. A schematic of this type of solder joint failure is shown in Figure 1.1.

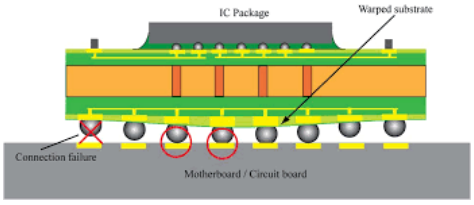

Figure 1.1: Warpage between package and PCB - solder disbond is highlighted

In light of the pivotal role of solder joints, it is easy to see why material characterization of solder joints has been a hot topic in the semiconductor industry since its inception. Modeling techniques that allow for more accurate simulations are constantly being researched by academia. The current best practice in the field of industrial solder joint modeling is using homogenized material models such as the Anand, Garofalo and Busso viscoplastic constitutive models. These models treat each solder joint as a homogeneous, isotropic continuum. In reality, however, solder joints are neither isotropic nor a continuum. For instance, state-of-the-art $SnAgCu$ (SAC) solder joints are composed of $\approx$ 95% highly anisotropic body centered tetragonal (BCT) $\beta - Sn$ crystals [5] which aggregate to form grains such as those visible in Figure 1.2. Given the minuscule size of these joints (a few hundred micrometers) and the low number of grains, microstructural effects become non-negligible [6]. Macroscopic modeling techniques are not capable of capturing the variability in mechanical properties caused by the variability in grain size and orientation. From a practical standpoint, being able to simulate this variability would lead to a more accurate range of early predictions for the lifetime of solder joints, thus providing better design margins before going to the product testing phase.

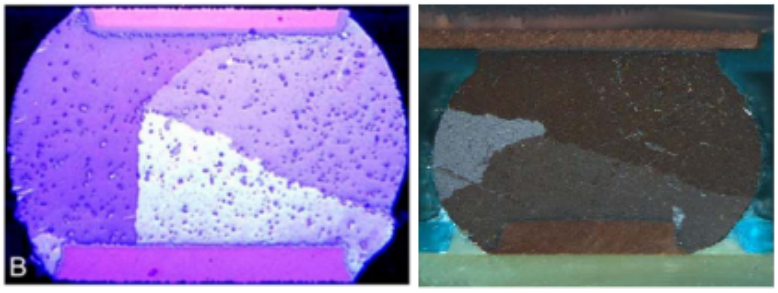

Figure 1.2: Cross-sections of two BGA solder joints showing granular microstructure [5] [7]

A recently-developed approach to solder joint modeling has been used in this thesis: this approach takes into account the microscopic anisotropy of solder joints by applying an anisotropic version of the Garofalo creep model to solder geometries that feature defined microstructures. These microstructures include randomly generated grains with different sizes and orientations, allowing for a statistical analysis of the effect of grain anisotropy. Furthermore, grain boundaries were also included in the simulations as interface elements.

These elements feature an isotropic, viscoplastic constitutive definition. All FE simulations in this project were performed in Marc Mentat.
Marc Mentat is a finite element analysis software that specializes in analyzing nonlinear situations, which frequently arise in the context of microelectronics modeling. In the case of solder joints, the main source of nonlinearity is the complex material behavior. It is also the FEA software of choice of the Package Innovation department within NXP Nijmegen. The wealth of experience the department has with Marc Mentat was a crucial factor towards the completion of this project. For reference, Marc is the actual solver software, while Mentat refers to the associated graphical user interface.

1.1. Research Objective

Reliability testing is a commonplace procedure in the semiconductor industry used to assess the operational durability of packages. Some standard procedures are Accelerated Thermal Cycling (ATC) and drop testing [8] [9]. These tests result in a statistical failure distribution. Simulation techniques are used to assess the solder joint lifetime and steer design developments accordingly. However, fully predicting the statistical distribution is not possible since Finite Element Modeling (FEM) simulations are deterministic in nature: simulating one product leads to one result.

The microstructure-based approach developed in this thesis aims to provide better predictions and explanations of the stochastic distributions that arise from reliability testing. Of course, this randomness in test results is due to a multitude of factors, such as small defects, testing conditions, moisture intrusions etc. Still, being able to quantify the influence of microstructural features on this randomness is a step forward in improving the usefulness of simulations.

As such, the objective of this thesis project is to develop and implement a microstructurally-informed solder joint modeling technique and use it to compute the distribution of Creep Strain Energy Density (CSED) developed in many unique microstructurally-defined solder joints during thermal cycling simulations. The CSED is a metric commonly associated with fatigue damage in solder joints [10]. Three different simulation campaigns were carried out to explore the effect of the microstructure in detail:

- Test 100 solder joints with a fixed microstructural geometry (number and shape of grains) with the only variable being the orientation of the grains. The objective of this campaign is to isolate the effect of the grain orientation on the solder joints.
- Test 100 solder joints with varying number of grains, grain size and orientations. These tests will provide an overview of the combined effect of all microstructure-related parameters.
- Test 30 different Wafer-Level Chip-Scale Package (WLCSP) sample products, each

fitted with a random combination of solder joints taken from the previous campaign. These tests are of a high practical utility as they can give an estimate of the effect of microstructural anisotropy on real-life applications.

The report is structured as to first explain the ”building blocks” of the microstructural modeling strategy, namely the material model used for the $\beta - Sn$ grains, the interface element approach used to model the grain boundaries and the Voronoi tessellations used to generate unique solder joint microstructures. The theoretical and numerical implementations of these components are discussed in chapter 2, along with validation of the numerical implementations where applicable. Chapter 4 describes how these building blocks were combined and used to set up the FE models of single solder joints. This chapter has a brief introduction where the software used throughout this project is presented, followed by FE simulation parameters and convergence studies. A validation of this set up is performed by means of recreation of a similar study found in the literature. The FE models generated according to the methods from this chapter were used to run the first two simulation campaigns. The set up used to prepare the third campaign is described in chapter 4. This set up is used to embed random combination of unique solder joints into a WLCSP product. It is worth noting that the set ups for both the single solder joints and the sample products had to be completely automated in order to generate the large amount of models required for the simulation campaigns. At last, the results of said campaigns are presented and discussed in chapter 5. The report is then concluded by final observations and recommendations for future work on the topic of this thesis.

2

Theory on Solder Joint Microstructure Modeling Techniques

The main objective of this project is to model the effect of microstructural variability on solder joint creep predictions. It is thus necessary to adopt a modeling strategy capable of representing the most important features of a solder joint's microstructure. In order to do so, the key features of an undamaged solder joint microstructure have been researched. An overview is provided in the next section.

2.1. Microstructure of Solder Joints

State-of-the-art solder joints are usually made of SAC alloys which include tin, silver and copper (SnAgCu) as their main constituents. Some modified versions including additional alloying elements such as zinc and bismuth in small percentages are also used in the industry to create so-called 'doped' alloys. However, this project will focus on the baseline SAC alloys given their widespread usage.

$\beta-Sn$ grains have a dominating effect on the thermomechanical response of SAC solder joints because of their large anisotropy and because of their $\approx$ 95% atomic percentage [11][12][13]. The anisotropy of $\beta - Sn$ crystals is due to their Body-Centered Tetragonal (BCT) crystal structure [5]. Because of this strong anisotropy, it is necessary to characterize the orientation of the Sn grains within the joints. The reflowing processes currently used to manufacture the solder joints result in $\beta - Sn$ grains with a near-random distribution of orientations [14].

The composition of the grains in the solder bulk is dependent on the alloy used as well as the choice of metallic substrate above and below the solder joint [15]. Figure 2.1 shows a typical SAC bulk structure featuring elongated $\beta - Sn$ grains embedded in an eutectic phase.

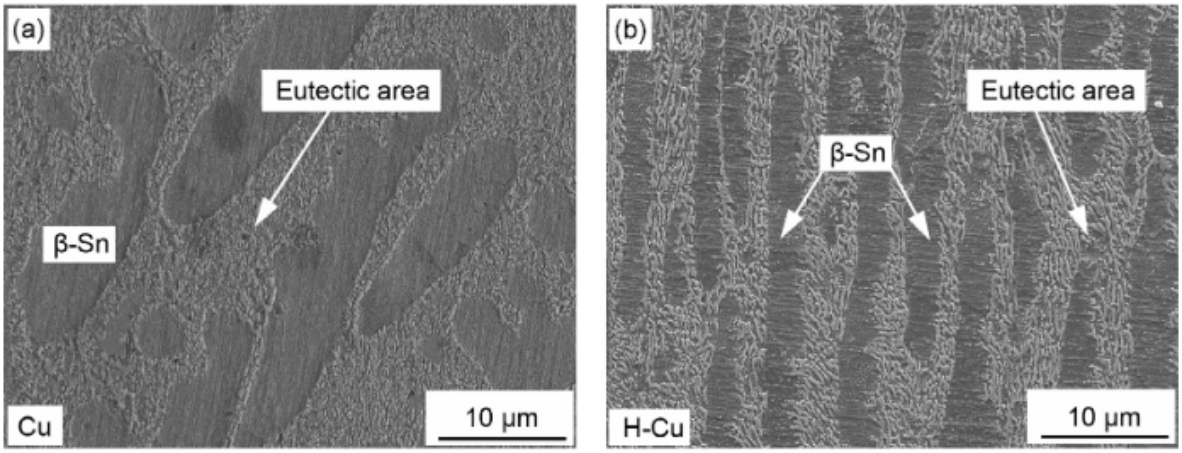

Figure 2.1: Microstructure of solder grains in SAC solder joints for two different substrates, from [15]

Henderson et al. [13] demonstrated via Polarized Light Microscopy (PLM) that the $\beta - Sn$ phase in SAC joints segregates in different grains according to clearly distinct crystallographic orientations (Figure 2.2). Typical BGA joints are composed of 1 to 12 independent $\beta - Sn$ grains, with an estimated average of 8 grains per joint [13].

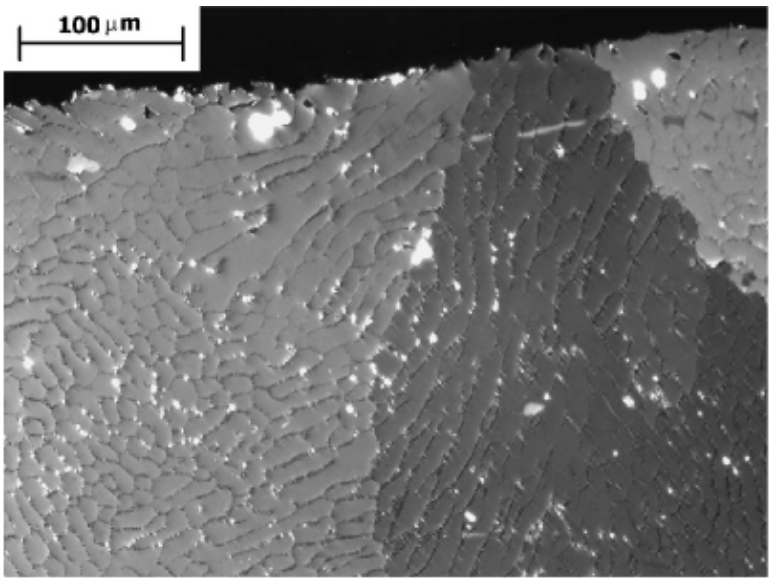

Figure 2.2: PLM image of a SAC solder joint. The contrast of each region reflects the crystallographic orientation of the $\beta - Sn$ phase. From [13]

The boundaries between the grains play an important role in the development of creep within the solder joint. In fact, creep in solder joints (and polycrystalline solids at large) is a complex phenomenon that combines diffusion and dislocation climb both within the grains and near the boundaries [16]. The creep behavior of grain boundaries is not nearly as well-researched as that of grains. The composition of grain boundaries tends to be more variable than that of the grains since alloying additives tend to segregate there [17]. Grain boundaries also play a critical role in the nucleation and propagation of fatigue cracks in the solder joints [18] [19] [20] and are therefore of interest to analyses of solder joint reliability. When subjected to

cyclic thermomechanical deformation, the $\beta - Sn$ grains dynamically recrystallize in the regions of higher inelastic deformation [13]. The new grain boundaries generated from this grain fragmentation process are sites of fatigue crack growth due to grain boundary sliding. This recrystallization process is outside the scope of this project, although it should be considered when developing microstructurally-informed damage progression models as a follow-up to this thesis.

Another important characteristic of the microstructure of SAC solder joints are the intermetallic compounds (IMC) that form at the top and bottom interfaces of the joint as well as in the bulk. The composition of these IMCs is determined by the surface plating material of the adjacent metallic pads. This surface plating then reacts with the solder bulk to form compounds [21], such as Ag_3Sn or the Cu_6Sn_5 IMCs shown in Figure 2.3 [13] [22]. The differences in IMC composition can lead to changes in mechanical properties, affecting the creep behavior of the solder joint [23]. Although the impact of IMCs at the interfaces on solder joint reliability has been acknowledged [24], they will not be included within the scope of the project in order to keep the complexity of the FE simulations within a tractable level.

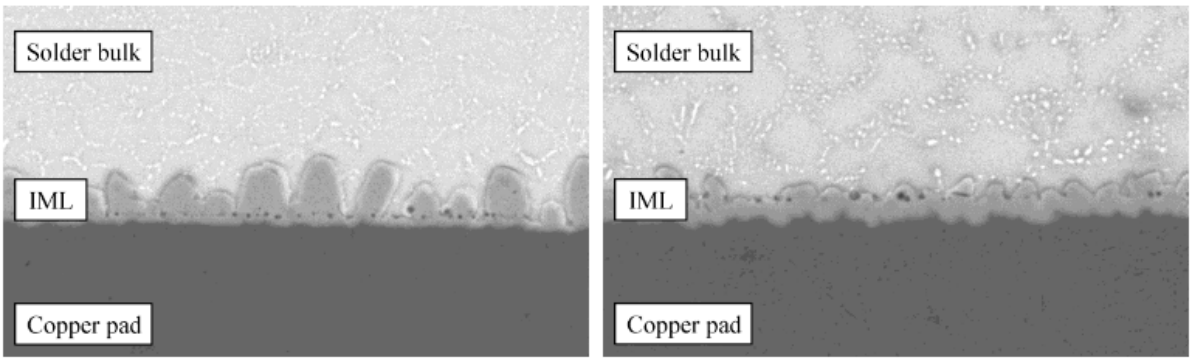

Figure 2.3: SEM images of Cu_6Sn_5 IMC at interface between SAC solder bulk and copper pad. The IMC is mentioned in the picture as IML (InterMetallic Layer). From [22]

This section has shown that solder joints feature highly complex, heterogeneous microstructures. The modeling strategy devised for this thesis addresses the main microstructural features in order to study the stochastic variability of solder joint creep response.

2.2. Microstructural Finite Element Modeling Strategy

The three key building blocks of the modeling strategy implemented in this project are:

- the $\beta - Sn$ grains;
- the boundaries between the grains;
- the random solder joint microstructural geometries featuring grains and grain boundaries.

These building blocks are presented in Figure 2.4 along with the respective techniques used to implement them.

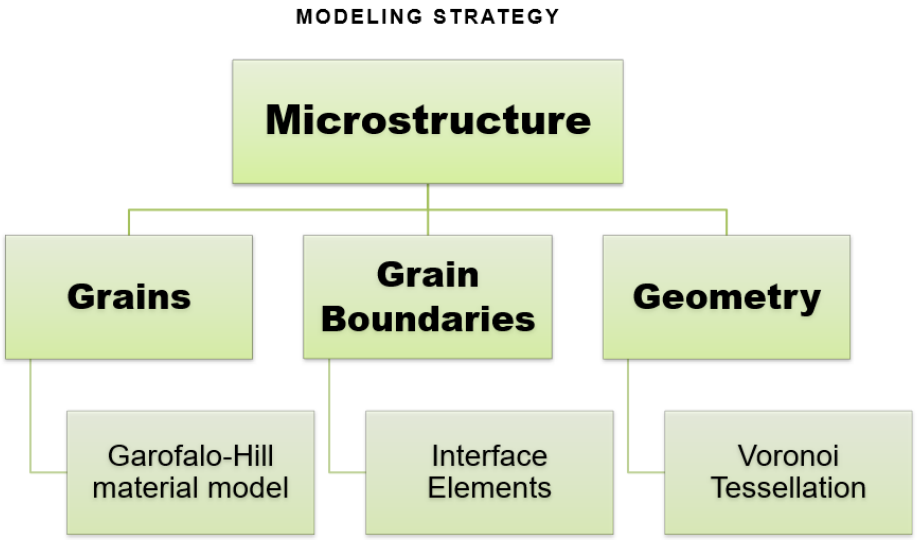

Figure 2.4: Overview of modeling strategy

This thesis explores a newly-developed modeling concept from academia, in which grains are modeled individually and given anisotropic properties. In particular, the Center for Advanced Life Cycle Engineering (CALCE) at the University of Maryland has developed a variant of the Garofalo creep model that implements anisotropy by replacing the von Mises equivalent stress with the Hill equivalent stress, its anisotropic counterpart [25]. The constitutive equations at the basis of this model are introduced in section 2.3.

The grain boundary creep modeling technique used in this project has also been adapted from work done at CALCE. Crossman et al. used a linear dependence between the displacement rate and the stress in numerical analyses of grain boundary behavior [26]:

$$\dot{u}_{GB} = (\frac{\delta}{\mu_B})\tau \tag{2.1}$$

The constitutive equation for the grain boundaries used in this thesis was developed by Jiang [27] starting from Crossman's analysis and is discussed in section 2.4. The Finite Element implementation of the grain boundaries has been carried out by means of zero-thickness interface elements.

The third component of the microstructural modeling strategy has to do with implementing the stochastic nature of solder joint microstructures in the simulations. In this project, the volume of a solder joint is partitioned in randomly-generated grains via Voronoi tessellations, also known as Voronoi diagrams. A 3D Voronoi tessellation subdivides a space into polyhedrons, where each polyhedron is the locus of points closest to a *seed*. More

information on the theory behind Voronoi diagram and their implementation in Finite Element software is given in section 2.5.

The remaining sections in this chapter will explain the theoretical background behind each of the three building blocks. Their implementation in the Finite Element software is also described along with the related validation procedures.

2.3. Grains: Garofalo-Hill Anisotropic Creep Constitutive Equations

The Garofalo-Hill constitutive model developed by CALCE combines the Garofalo creep constitutive relation with the equivalent Hill stress formulation. The Garofalo creep model calculates the steady-state creep rate, which makes up most of the creep life of solder joints, see Figure 2.5.

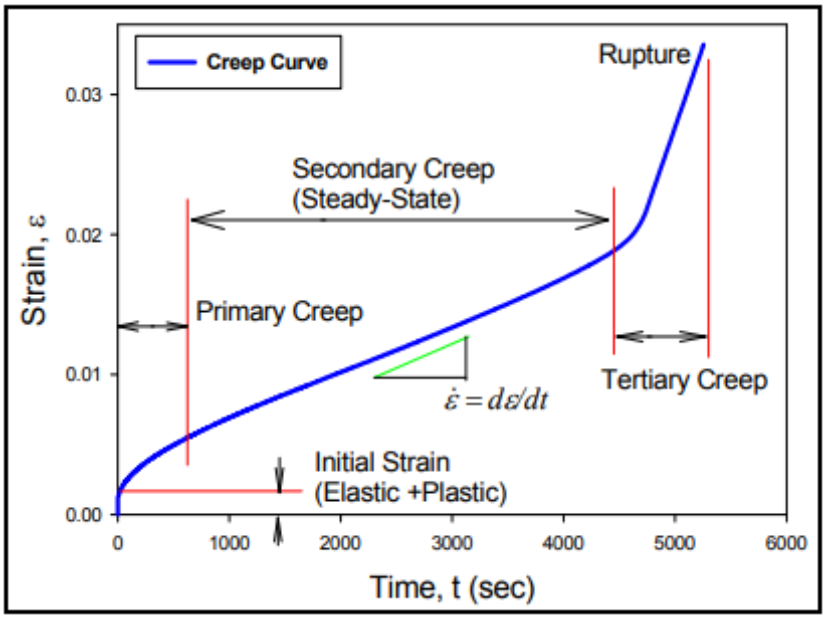

Figure 2.5: Typical solder joint creep curve. From [28]

Plasticity is not accounted for in the model, although this is not a significant drawback: in many practical conditions for solder joints creep deformation is orders of magnitude larger than plastic deformation [29].

The original hyperbolic sine Garofalo relation has been used to compute steady-state creep at high temperatures and stress magnitudes. Power law formulations usually ”break down” at these regimes [30]. As creep is a time-dependent phenomenon, the main constitutive equation of a creep constitutive model relates the stress with the creep strain *rate*. These equations are known as *flow rules*. The flow rule of the Garofalo constitutive model is [31]:

$$\dot{\epsilon_{cr}} = C_1[sinh(C_2\sigma_{vm})]^{C_3}e^{-\frac{C_4}{T}} \tag{2.2}$$

where $\dot{\epsilon_{cr}}$ is the creep strain rate, σ_{vm} is the von Mises equivalent stress, T is the temperature in K and C_1, C_2, C_3, C_4 are material parameters.
The Garofalo-Hill variant replaces the von Mises stress with its anisotropic counterpart: the Hill stress. The Hill stress is defined as:

$$\sigma_{Hill} = \sqrt{F(\sigma_{22}-\sigma_{33})^2 + G(\sigma_{33}-\sigma_{11})^2 + H(\sigma_{11}-\sigma_{22})^2 + 2L\sigma_{23}^2 + 2M\sigma_{13}^2 + 2N\sigma_{12}^2} \tag{2.3}$$

where F, G, H, L, M and N are the Hill constants, derived for the current state of anisotropy [32]. Using the Hill stress in Equation 2.2 yields the equivalent Hill creep strain rate:

$$\dot{\epsilon}_{Hill}^{cr} = C_1(sinh(C_2\sigma_{Hill}))^{C_3}exp(\frac{-C_4}{T}). \tag{2.4}$$

The equivalent strain rate is then used to obtain the creep strain rate tensor by multiplying it with the gradient to the Hill stress:

$$\dot{\epsilon}_{ij}^{cr} = \dot{\epsilon}_{Hill}^{cr}\frac{\delta\sigma_{Hill}}{\delta\sigma_{ij}} \tag{2.5}$$

Lastly, the Garofalo-Hill model is coupled with a corresponding anisotropic linear elastic behavior.

2.3.1. Numerical Implementation of Garofalo-Hill Equations

The Garofalo-Hill has been implemented in Marc Mentat by combining two features present in stock Marc: the explicit Garofalo creep formulation and the Hill plasticity. The Hill plasticity setting is not actually used to introduce a definition for plasticity in the model; rather, it serves to provide a definition for the equivalent Hill stress σ_{Hill}. Plasticity can be safely ignored as the contribution of plasticity to the total inelastic deformation is negligible when compared to that of creep [33]. Plasticity is removed from the Marc model by means of setting the yield stress of the material at an extremely high value. Marc uses the Maxwell material representation, in which the strain rate is considered the sum of its elastic, plastic and creep components, see Figure 2.6. As plasticity is discarded, the total strain rate becomes:

$$\dot{\epsilon}_{tot} = \dot{\epsilon}^{el} + \dot{\epsilon}^{cr} \tag{2.6}$$

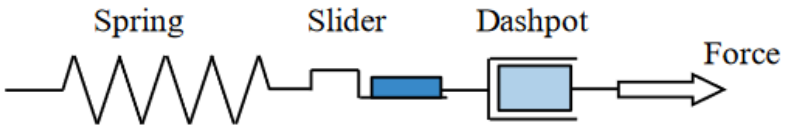

Figure 2.6: Maxwell material representation. The spring gives the elastic deformation, the slider plastic deformation and the dashpot creep. The force (stress) acting on each element is the same while the strains are additive. From [34]

In total, the material definition of the $\beta - Sn$ grains in Marc is a sum of three settings: anisotropic elasticity, an anisotropic definition of the equivalent stress and the Garofalo creep formulation. These three settings and the values used in their parameters are shown in Figure 2.7, Figure 2.8 and Figure 2.9.

Figure 2.7: Elastic properties of grain material model (moduli expressed in MPa)

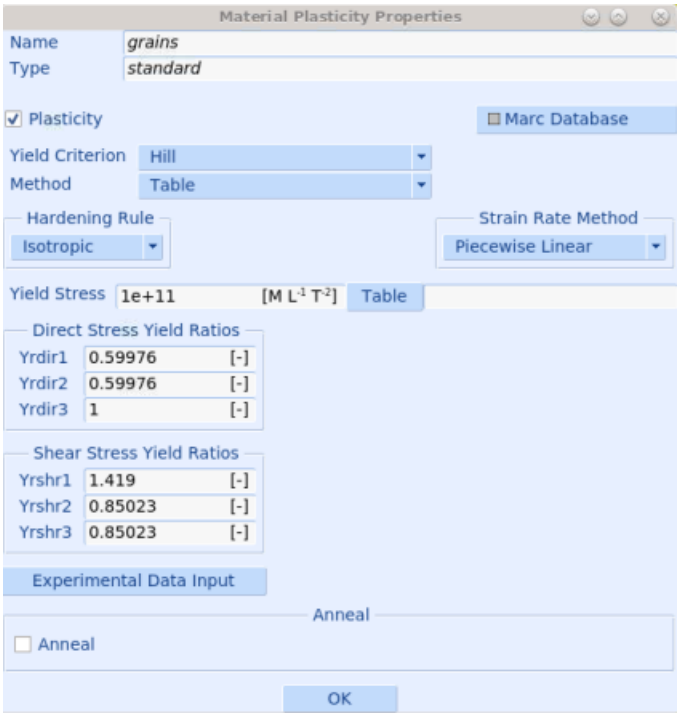

Figure 2.8: Hill anisotropy constants for grain material model

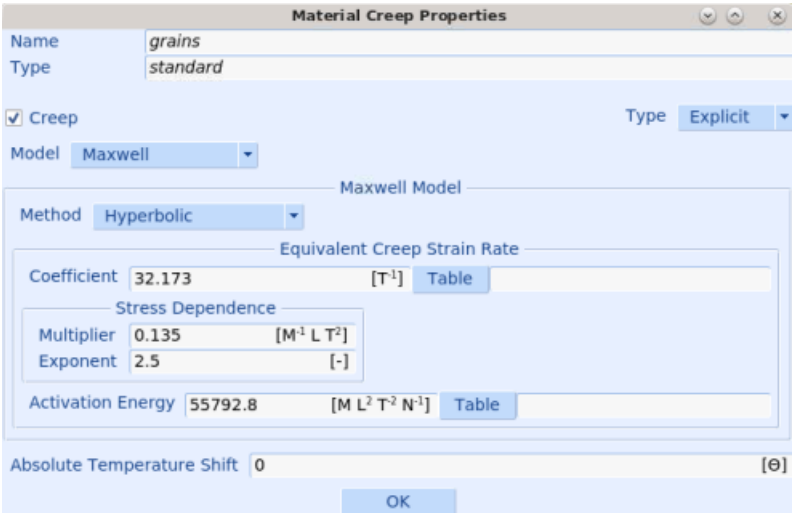

Figure 2.9: Garofalo creep constants for grain material model

The Marc implementation of the Garofalo-Hill model described in this section uses a purely explicit formulation. This may become a drawback, as explicit formulations are usually restrictive when it comes to permitted time steps. To this purpose an implicit implementation has been partially developed. However, this version does not yet feature a definition for anisotropic elasticity and as such it could not be used in this project. Nonetheless, this implicit formulation could lead to computational benefits in the future, once it is upgraded with a definition for anisotropic elasticity. This formulation may be found in Appendix A.

2.3.2. Validation of Garofalo-Hill Implementation

The validation of the Garofalo-Hill implementation is performed on the rod model depicted in Figure 2.10. The model is clamped on one end while the other end is subject to a constant tensile stress of 5 MPa. Different material orientations are tested.

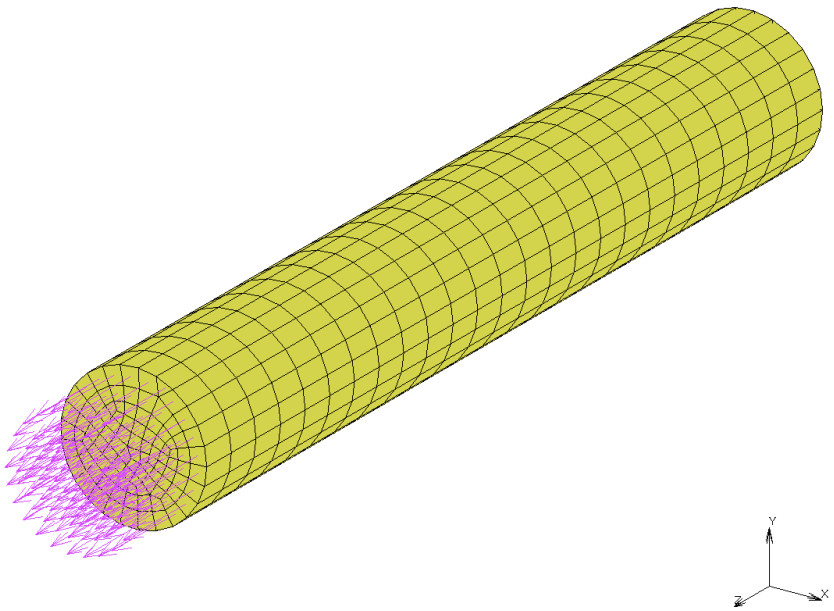

Figure 2.10: Rod geometry used to test Garofalo-Hill implementation. A constant stress is applied along the global z-axis

Three different material orientations are tested: in the first one the local and global axes coincide, in the second one the material y-axis is aligned with the global z-axis and in the third one the material z-axis is rotated by 45°around the global y-axis w.r.t. the global z-axis. The measured output is the creep strain rate tensor in the three global axes. All tensors used in the following calculations are indicated in Voigt notation. The testing temperature is constant at 125 °C. The values for the model constants have been taken from the work of Jiang [27], from which the Garofalo-Hill model itself has also been taken.

The creep strain rate is computed according to Equation 2.3, Equation 2.4 and Equation 2.5. The Hill stress gradient in Equation 2.5 is equal to:

$$\frac{\partial \sigma_{Hill}}{\partial \sigma_{ij}} = \begin{bmatrix} \frac{(G+H)\sigma_{11} - G\sigma_{33} - H\sigma_{22}}{\sigma_{Hill}} \\ \frac{(F+H)\sigma_{11} - F\sigma_{33} - H\sigma_{22}}{\sigma_{Hill}} \\ \frac{(G+F)\sigma_{33} - F\sigma_{22} - G\sigma_{11}}{\sigma_{Hill}} \\ \frac{2L\sigma_{23}}{\sigma_{Hill}} \\ \frac{2M\sigma_{13}}{\sigma_{Hill}} \\ \frac{2N\sigma_{12}}{\sigma_{Hill}} \end{bmatrix} \tag{2.7}$$

Case 1: global and material coordinate systems coincide

The applied stress results in an almost perfectly homogeneous stress field inside the rod. Still, a point far from the boundary conditions is chosen for the measurements. At this point, σ_{33}=5.007 MPa while all other stress components are zero. Equation 2.3 yields σ_{Hill}=5 MPa. The Hill stress is then used to compute the equivalent creep strain rate:

$$\dot{\epsilon}^{cr}_{Hill} = 32.17(sinh(0.135\sigma_{Hill}))^{2.5} exp(\frac{-55793}{8.314 * 398.15}) = 6.97 * 10^{-7}\frac{1}{s} \tag{2.8}$$

While the stress gradient is:

$$\frac{\partial \sigma_{Hill}}{\partial \sigma_{ij}} = \begin{bmatrix} \frac{(0.5+2.28)\sigma_{11} - 0.5\sigma_{33} - 2.28\sigma_{22}}{\sigma_{Hill}} \\ \frac{(0.5+2.28)\sigma_{11} - 0.5\sigma_{33} - 2.28\sigma_{22}}{\sigma_{Hill}} \\ \frac{(0.5+0.5)\sigma_{33} - 0.5\sigma_{22} - 0.5\sigma_{11}}{\sigma_{Hill}} \\ \frac{2*2.075\sigma_{23}}{\sigma_{Hill}} \\ \frac{2*2.075\sigma_{13}}{\sigma_{Hill}} \\ \frac{2*0.745\sigma_{12}}{\sigma_{Hill}} \end{bmatrix} = \begin{bmatrix} -0.5 \\ -0.5 \\ 1 \\ 0 \\ 0 \\ 0 \end{bmatrix} \tag{2.9}$$

Combining the two results in the creep strain rate tensor:

$$\dot{\epsilon}^{cr}_{ij} = \begin{bmatrix} -3.49 * 10^{-7} \\ -3.49 * 10^{-7} \\ 6.98 * 10^{-7} \\ 0 \\ 0 \\ 0 \end{bmatrix} \frac{1}{s} \tag{2.10}$$

The creep strain in the z-direction is then extracted from Marc and divided by the total loadcase time (2000 s) to obtain the creep strain rate. This is possible because a constant stress corresponds to a linear creep strain.

Dividing the total creep stain by the total loadcase time yields:

$$1.386 * 10^{-3}/2000 = 6.93 * 10^{-7} \tag{2.11}$$

Which comes within 0.7% of the analytical prediction. The creep strain rates for the material x- and y-directions have been found to be :

$$-6.93 * 10^{-7}/2000 = -3.465 * 10^{-7} \tag{2.12}$$

Again within 0.7% of the analytical calculations.

Case 2: material y-axis and global z-axis are aligned

For this case and case 3, a new notation is used to identify the stresses and strain in the global and material coordinate systems as these are now different. The subscript m stands for material coordinate system while g stands for global. In this case, there is an applied σ_{33g} of 5 MPa which translates to σ_{22m}=5 MPa. All other stress components in the material coordinate system are zero. The Hill stress gradient for this case then is:

$$\frac{\partial \sigma_{Hill}}{\partial \sigma_{ij}} = \begin{bmatrix} -1.37 \\ 1.67 \\ -0.29 \\ 0 \\ 0 \\ 0 \end{bmatrix} \tag{2.13}$$

The Hill stress (which is computed from the stress components in the material coordinate system) is equal to 8.44 MPa, leading to an equivalent creep strain rate of 3.58*10^{-6} 1/s. Again, combining the equivalent creep strain rate with the Hill stress gradient results in the creep strain rate tensor:

$$\dot{\epsilon}^{cr}_{ij_m} = \begin{bmatrix} -4.89 * 10^{-6} \\ 5.97 * 10^{-6} \\ -1.07 * 10^{-6} \\ 0 \\ 0 \\ 0 \end{bmatrix} \frac{1}{s} \tag{2.14}$$

The creep strains calculated by Marc are extracted and compared with the analytical results in Table 2.1. The results are satisfyingly close. Two creep strain rate components have a slightly higher discrepancy than the previous orientation at $\approx$ 2.5%.

Table 2.1: Creep strain rate (CSR) component comparison for second material orientation

Component in global CS	Component in local CS	Analytical CSR (1/s)	FEM CSR (1/s)
$\dot{\epsilon}_{11_g}$	$\dot{\epsilon}_{11_m}$	-4.77*10^{-6}	-4.89*10^{-6}
$\dot{\epsilon}_{22_g}$	$\dot{\epsilon}_{33_m}$	-1.05*10^{-6}	-1.07*10^{-6}
$\dot{\epsilon}_{33_g}$	$\dot{\epsilon}_{22_m}$	5.82*10^{-6}	5.97*10^{-6}

Case 3: material CS rotated 45°around y-axis w.r.t. global CS

The last material orientation results in σ_{11_m} = σ_{33_m} = 2.5 MPa. For the first time, a shear stress component is also present in the material, with σ_{31_m} = 2.5 MPa. All other components of the

stress tensor in material coordinates are zero, leading to σ_{Hill} = 6.615 MPa. The associated equivalent creep strain rate is $\dot{\epsilon}^{cr}_{Hill}$ = 1.605*10^{-6} 1/s. The Hill stress gradient for this test condition is:

$$\frac{\partial \sigma_{Hill}}{\partial \sigma_{ij}} = \begin{bmatrix} 0.87 \\ -1.06 \\ 0.19 \\ 0 \\ 0 \\ 1.58 \end{bmatrix} \tag{2.15}$$

which is then multiplied with $\dot{\epsilon}^{cr}_{Hill}$ to obtain the creep strain rate tensor:

$$\dot{\epsilon}^{cr}_{ij_m} = \begin{bmatrix} 1.39 * 10^{-6} \\ -1.69 * 10^{-6} \\ 3.03 * 10^{-7} \\ 0 \\ 0 \\ 2.52 * 10^{-6} \end{bmatrix} \frac{1}{s} \tag{2.16}$$

Since the x- and z-axes in the material CS are not aligned to any axes in the global CS, it is necessary to transform the components of the creep strain rate tensor that have been calculated for the material CS to the global CS. The rotation matrix for a rotation around the y-axis is:

$$R_y(\theta) = \begin{bmatrix} cos(\theta) & 0 & sin(\theta) \\ 0 & 1 & 0 \\ -sin(\theta) & 0 & cos(\theta) \end{bmatrix} \tag{2.17}$$

The creep strain rate tensor is then expressed in global coordinates by means of:

$$\dot{\epsilon}^{cr}_{ij_g} = R_y \dot{\epsilon}^{cr}_{ij_m} R_y^T \tag{2.18}$$

It is important to mention that, in order for the rotation to be successful, the tensorial definition of the shear strain must be used. This amounts to half of the commonly used shear strain definition (which is also the quantity Marc works with). By using this definition of shear strain and rotating the creep strain rate tensor, we obtain:

$$\dot{\epsilon}^{cr}_{ij_g} = \begin{bmatrix} -4.17 * 10^{-7} \\ -1.69 * 10^{-6} \\ 2.11 * 10^{-6} \\ 0 \\ 0 \\ 1.09 * 10^{-6} \end{bmatrix} \frac{1}{s} \tag{2.19}$$

where the shear component $\dot{\epsilon}^{cr}_{31_g}$ has already been doubled to match the traditional definition of shear strain. Table 2.2 shows the comparison between analytical and FE results, which is again satisfactory.

Table 2.2: Creep strain rate (CSR) component comparison for third material orientation

Component in global CS	Analytical CSR (1/s)	FEM CSR (1/s)
$\dot{\epsilon}_{11_g}$	-4.17*10^{-7}	-4.13*10^{-7}
$\dot{\epsilon}_{22_g}$	-1.69*10^{-6}	-1.67*10^{-6}
$\dot{\epsilon}_{33_g}$	2.11*10^{-6}	2.09*10^{-6}
$\dot{\epsilon}_{31_g}$	1.09*10^{-6}	1.07*10^{-6}

2.4. Grain Boundaries: Constitutive Equations

The modeling strategy described at the beginning of this chapter mentions the explicit use of grain boundaries in the simulations. Grain boundaries will be represented by interface elements fitted with an isotropic elastic-viscoplastic constitutive model developed by Jiang [27]. Current practice methods in solder joint modeling usually represent the solder as an homogeneous continuum; in the few instances in which grain boundaries are modeled they are usually modeled as very thin layers of solid elements [35]. The interface element approach has been recently used to successfully model integranular fracture in polycrystalline solids [36][37]. Still, damage and fracture behavior of the solder go beyond the scope of this project. The interface elements are therefore used to model the undamaged behavior of the grain boundaries. Implementation of a damage parameter in the interface elements might be of interest for future projects, more on this in section 6.1.

Previous research on creep of pure Sn and Sn-based alloys has found a linear dependence of the equivalent creep strain rate on the equivalent stress at a given temperature [26] [38]:

$$\dot{\bar{\epsilon}}^{cr} = A_{GB}\bar{\sigma} \tag{2.20}$$

where A_{GB} is a unified parameter representing the influence of multiple factors such as thickness and temperature. Practically, A_{GB} was determined by Jiang through comparison with physical experimental measurements, resulting in a value of $1.05 * 10^{-6}$ s/MPa at room temperature. Currently, values for A_{GB} at different temperatures are not available. In addition to creep the formulation of this model also includes isotropic elasticity with a Young's Modulus E of 70 GPa and a Poisson's ratio ν of 0.33. The properties have been taken from Jiang [27].

2.4.1. Numerical Implementation of Grain Boundary Model

In order to be used in numerical simulation software the grain boundary model (referred to as GB model from now on) must be approximated numerically and then implemented in Marc via a custom piece of code. Marc is written in the FORTRAN programming language. It is possible for a Marc user to add custom functionalities to Marc by replacing default "blocks" of

Marc code with their own code. These blocks are known as **subroutines** and cover an extremely wide range of features. Multiple subroutines have been developed and used throughout this project. The suitable subroutine for this task is UCOHESIVE, which allows the user to define a custom constitutive model for an interface element in the from of a traction-separation law. As such, *tractions* and *displacements* are used to model the material behavior instead of stresses and strains. As the cohesive elements have no actual thickness, only three traction components are defined: one in the normal direction and two in the in-plane shear directions. Whenever needed for calculations, all other traction components are assumed to be zero.

The required outputs of UCOHESIVE are the stress at the end of the increment σ^{i+1} and the matrix **D** which describes the relationship between the stress vector σ_{ij} and the displacement vector u_{ij}:

$$\sigma_{ij} = \mathbf{D} u_{ij} \tag{2.21}$$

There is a disconnect between the constitutive model described by Equation 2.20 and the formulation used in UCOHESIVE. The former uses strains, while the latter uses displacements. The strain is equal to the displacement divided by the initial grain boundary thickness; however, the interface elements have no thickness. It is thus necessary to define a *constitutive thickness*, which is simply a fictitious thickness used for calculations. Methods in the literature recommend using a constitutive thickness of $1\mu m$ rather than the real thickness of the grain boundary in order to facilitate computations [26]. The elasticity and creep constitutive relations must be therefore accordingly modified before they can be used in UCOHESIVE:

$$\dot{\epsilon}^{cr} = A_{GB}\sigma --> \frac{\dot{u}^{cr}}{t_{cz}} = A_{GB}\sigma --> \dot{u}^{cr} = A_{GB} t_{cz} \sigma \tag{2.22}$$

$$\sigma = E\epsilon^{el} --> \sigma = E\frac{u^{el}}{t_{cz}} --> \sigma = \frac{E}{t_{cz}} u^{el} \tag{2.23}$$

This means that A_{GB} and E will have to be multiplied and divided respectively by the constitutive thickness when they are used in UCOHESIVE.
The derivation to obtain σ^{i+1} starts by applying Hooke's law to Equation 2.20:

$$\dot{\epsilon}_{cr} = A_{GB} * E\epsilon_{el} = A_{GB} * E(\epsilon_{tot} - \epsilon_{cr}) \tag{2.24}$$

The equation above is time-discretized by integrating over an increment:

$$\int_{t_i}^{t_{i+1}} \dot{\epsilon}_{cr} dt = A_{GB} * E \int_{t_i}^{t_{i+1}} (\epsilon_{tot} - \epsilon_{cr}) dt \tag{2.25}$$

In order to integrate the left-hand side of Equation 2.25 an assumption is made that the strain rate is constant over the interval. On the right-hand side, the total and elastic strains are

approximated by the midpoint rule, in which the average of the strains at the beginning and at the end of the increment is used as the value of the strain for the increment. It is worth noting that this is an implicit integration rule as the term ϵ_{cr}^{i+1} will now appear in both sides of the equation.

$$\Delta\epsilon_{cr} = \epsilon_{cr}^{i+1} - \epsilon_{cr}^{i} = A_{GB} * E(\frac{\epsilon_{tot}^{i+1} + \epsilon_{tot}^{i}}{2} - \frac{\epsilon_{cr}^{i+1} + \epsilon_{cr}^{i}}{2})\Delta t \tag{2.26}$$

Isolating ϵ_{cr}^{i+1} results in:

$$\epsilon_{cr}^{i+1} = \frac{\frac{A_{GB}E\Delta t}{2}}{1 + \frac{A_{GB}E\Delta t}{2}}(\epsilon_{tot}^{i+1} + \epsilon_{tot}^{i}) + \frac{1 - \frac{A_{GB}E\Delta t}{2}}{1 + \frac{A_{GB}E\Delta t}{2}}\epsilon_{cr}^{i} \tag{2.27}$$

Finally, the stress at the end of the increment σ^{i+1} is obtained through Hooke's law:

$$\sigma^{i+1} = E(\epsilon_{tot}^{i+1} - \epsilon_{cr}^{i+1}) \tag{2.28}$$

It is important to note that the above derivation refers to a single stress/strain component. The original constitutive model deals in terms of equivalent tractions and displacements; to convert them to components it is necessary to multiply the equivalent stress by the stress gradient $\frac{\partial\sigma_{eq}}{\partial\sigma_{ij}}$. σ_n denotes the normal stress component while τ_1 and τ_2 denote the in-plane shear stress components.

$$\dot{\epsilon_{ij}^{cr}} = A_{GB}\bar{\sigma}\frac{\partial\sigma_{eq}}{\partial\sigma_{ij}} \qquad where \qquad \frac{\partial\sigma_{eq}}{\partial\sigma_{ij}} = \begin{bmatrix} \frac{\sigma_n}{\sigma_{eq}} \\ \frac{3\tau_1}{\sigma_{eq}} \\ \frac{3\tau_2}{\sigma_{eq}} \end{bmatrix} \tag{2.29}$$

The terms σ_n, τ_1, τ_2 refer to the three stress components. The equivalent stress $\bar{\sigma}$ is simply a modified version of the von Mises stress in which the missing components are treated as zeroes:

$$\sigma_{eq} = \sqrt{2\sigma_n^2 + 6(\tau_1 + \tau_2)^2} \tag{2.30}$$

In concrete terms, this means that from Equation 2.25 to Equation 2.29 A_{GB} will be $1.05 * 10^{-6}$ for the normal component and $3 * 1.05 * 10^{-6}$ for the two shear components. Lastly, E represents the Young's Modulus for the normal component and the Shear Modulus for the shear components.

The **D** matrix represents the the tangent stiffness matrix. Since there is no coupling between stresses and strains in different directions, **D** is a diagonal matrix with three elements. These elements are found by taking the derivative of one stress component with the corresponding strain. For instance, the normal component of the tangent stiffness matrix is:

$$\mathbf{D}_{11} = E(1 - (\frac{\frac{A_{GB}E\Delta t}{2}}{\frac{1+A_{GB}E\Delta t}{2}}) \tag{2.31}$$

Since interface elements have zero thickness, they cannot accommodate any compressive deformation as that would lead to interpenetration of the joined solid elements. In theory, this means that their stiffness in compression is infinite. Intuitively, a numerical simulation software cannot handle an infinite value, so a very high number has to be used instead. This number cannot just be arbitrarily high: when compression is imposed on the interface element, the stress that generates within the element is proportional to the stiffness. Exceedingly high stress magnitudes might lead to convergence issues with the FEM simulations. A compressive stiffness of $5 * 10^6$ GPa has been found to be a good compromise. With regards to creep, the constant A_{GB} is zeroed when the grain boundary is under compression.

2.4.2. Validation of Grain Boundary Model

The validation of the GB model was carried out by means of a simple MARC model featuring two clamps joined by a layer of cohesive elements, shown in Figure 2.11. Three separate loading conditions have been analyzed: constant tension, linearly increasing tension and cyclic tension/compression. The stress-strain curves generated by Marc are compared with the analytical solution which was developed in Python.

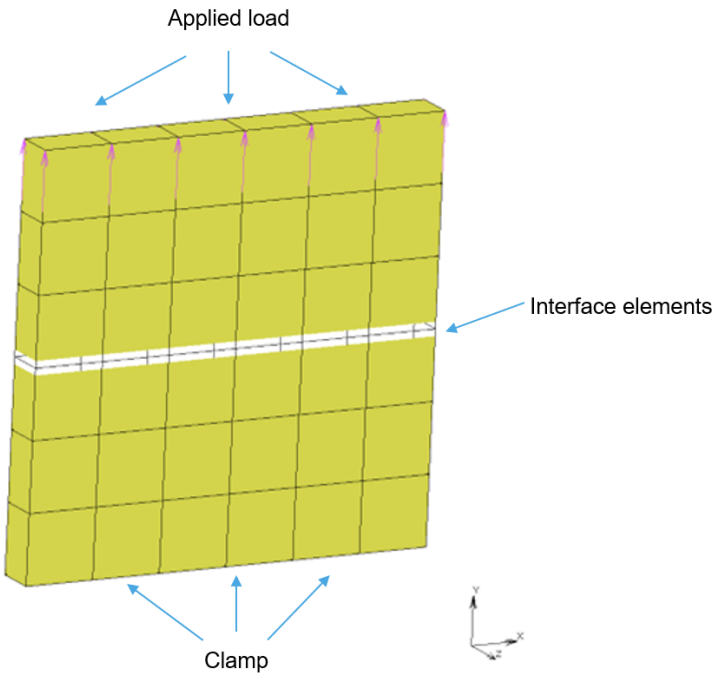

Figure 2.11: MARC model used to validate the grain boundary constitutive model. The cohesive elements are at the middle of the model.

The lower edge of the geometry in Figure 2.11 is fully clamped while the imposed displacement (tension, compression or shear) is applied to the nodes at the top edge.

Constant Tension

In the first case a constant tensile stress of 1 MPa is applied. An arbitrary value of the Young's modulus is used; in this case it is 5 GPa. The output of interest is the strain in the normal direction at one of the cohesive elements. Marc computes elastic strains during the so called "increment 0", i.e. before the first increment starts. Since there is an applied stress at the beginning of the simulation, the strain calculated by Marc reads $1MPa/5000MPa = 0.0002$. This strain is not computed by the analytical solution, which accounts only for creep. Therefore, the elastic displacement must be subtracted from the Marc output before it may be compared to the analytical solution.

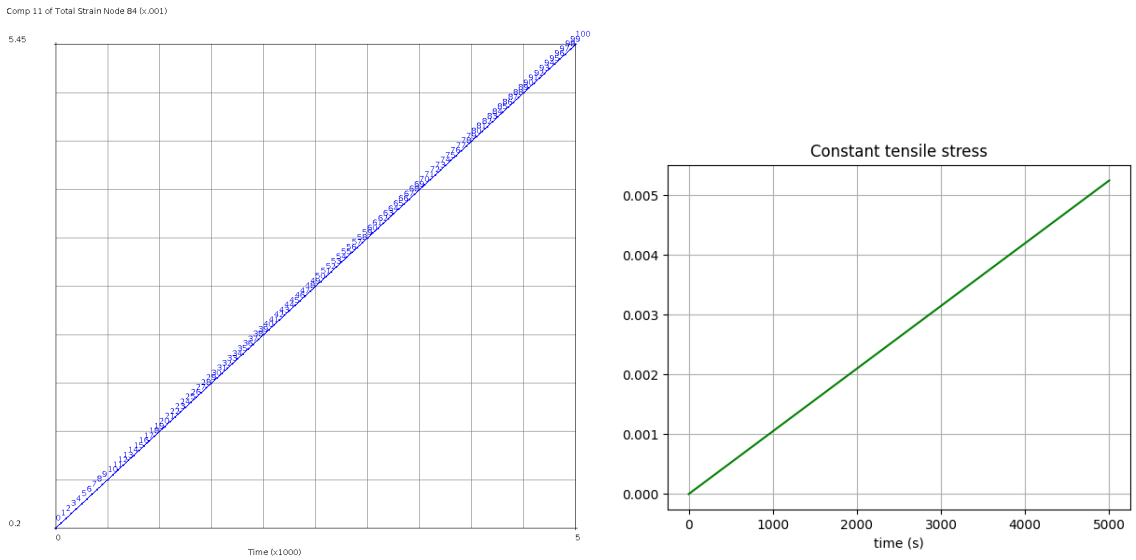

Figure 2.12: FEM (left) and analytical (right) strain vs. time curves. Time in seconds

The maximum strain in the analytical solution amounts to 0.00525, matching the creep computed by Marc. Only one time step has been analyzed since, as long as the strain is linear, the solution is exact due to the midpoint rule used in Equation 2.26.

Linearly Increasing Tension

Now the tensile stress is linearly increased from 0 to 1 MPa over the course of the simulation. This means that there is no elastic strain at the beginning of the simulation: the elastic strain is added on top of the creep strain as the simulation progresses. The Young's modulus stays the same at 5 GPa; therefore the total elastic strain is still 0.0002.

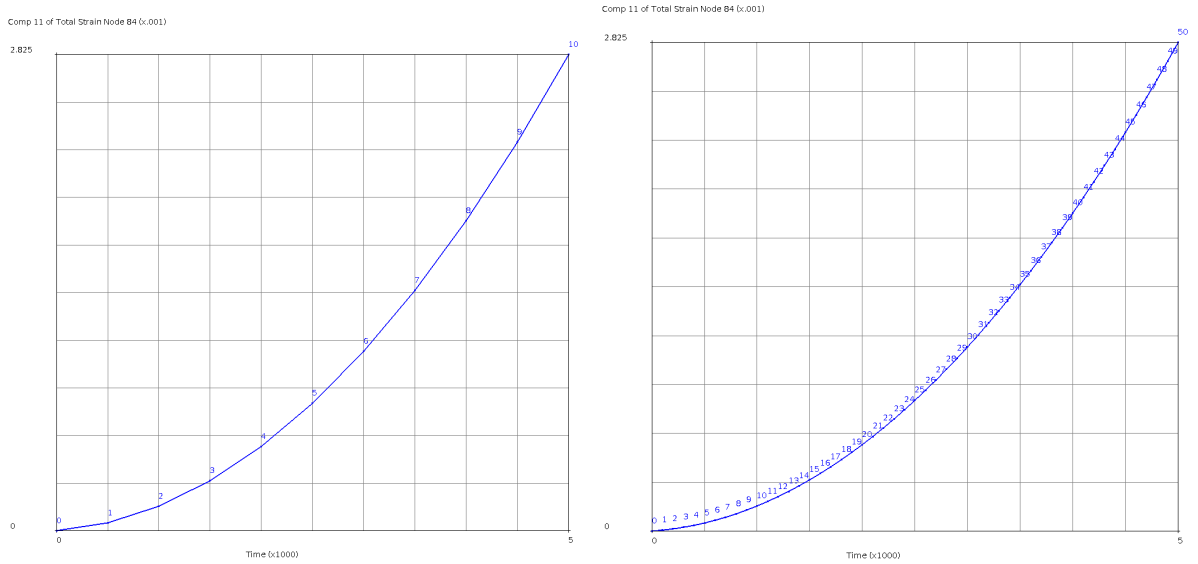

Figure 2.13: Strain vs. time curves (time in seconds) from MARC. Left: $\Delta t = 500s$, right: $\Delta t = 100s$

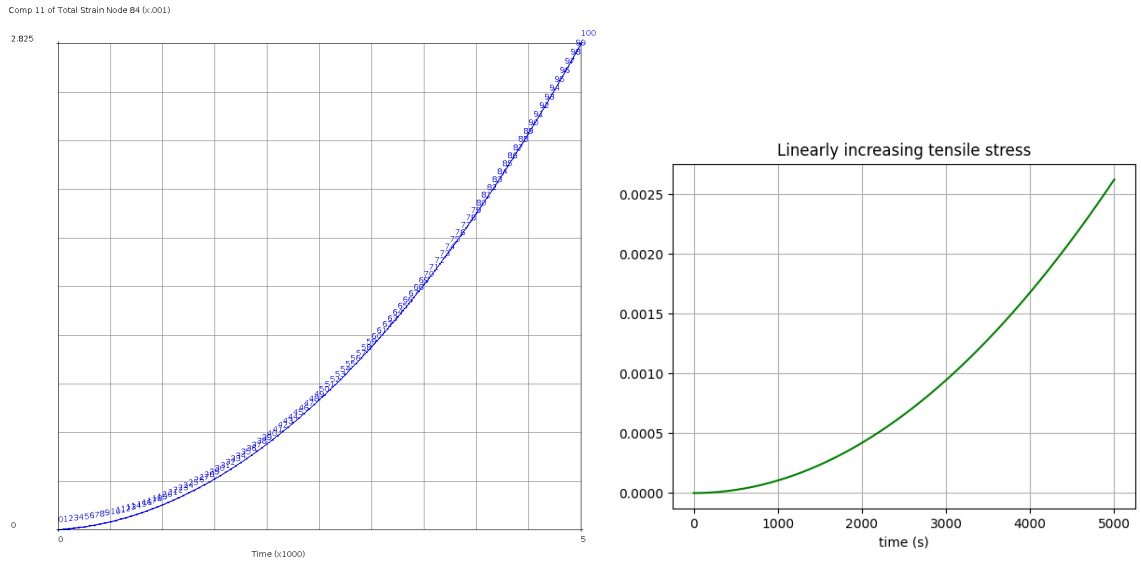

Figure 2.14: Strain vs. time curve from MARC for $\Delta t = 50s$ (left) and analytical strain vs. time curve (right). Time in seconds

Cyclic tension/compression

This loadcase was tested to qualitatively verify that compression on the grain boundaries does not generate interpenetration in the interface elements. An alternating compressive/tensile displacement is applied on the top edge of the geometry. The loading profile is shown in Figure 2.15a. The displacements actually applied to the geometry are those shown in the profile times 0.01, in mm. The response of the interface elements in terms of normal strain is given in Figure 2.15b. The negative displacement during compression (interpenetration) is

negligible as the displacement is entirely accommodated by the solid elements rather than the interface elements. The increased compressive stiffness is triggered when both the stress and the current strain on the interface element are negative. This allows the element to expand again when the applied compression turns to tension.

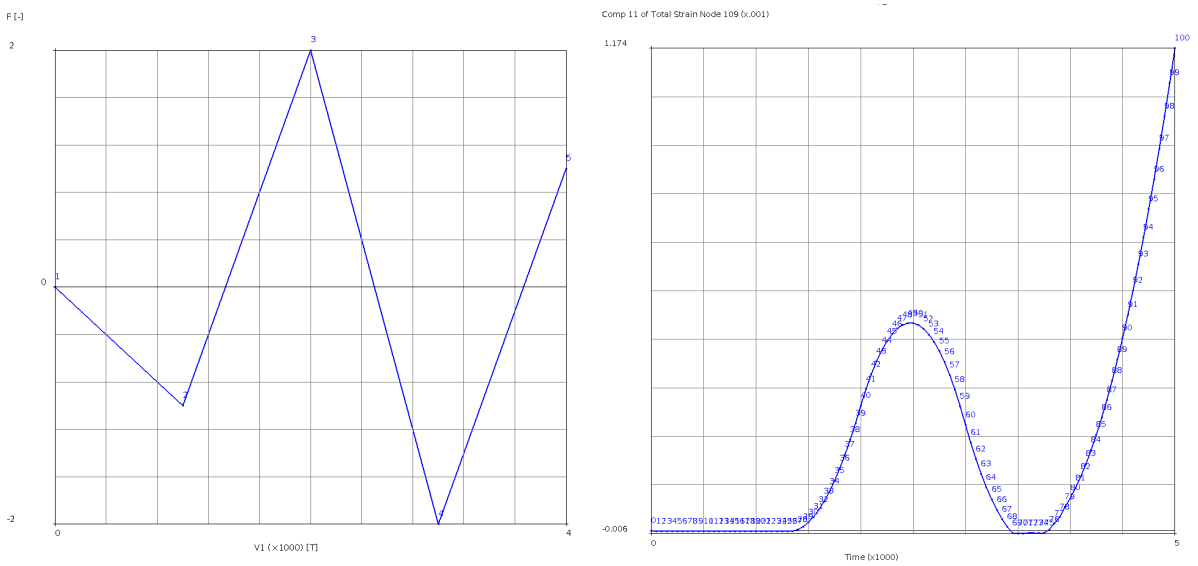

(a) Profile of applied displacement

(b) Strain vs time response of interface element

Figure 2.15: Cyclic tensile/compressive loadcase

2.5. Microstructural Geometry: Voronoi Tessellation

Current package soldering processes such as solder reflow are not yet capable of reliably achieving an intended microstructure in the finished solder joint [13]. This variability in solder joint microstructure must be accounted for, both in terms of number, size and crystallographic orientation of the main-phase Sn grains. To this purpose, the third and last building block of the microstructural modeling strategy is a 3D space partitioning method capable of representing the random grain distributions in different solder joints. This method is explained in this section and it is known as *Voronoi tessellation*.

Figure 2.16: A 2D Voronoi tessellation. Each of the 20 colored cells is associated to one seed (black dots). Taken from Wikipedia

A Voronoi tessellation, also known as Voronoi diagram, is a 2D or 3D diagram that divides a space into regions so that each region is made up of all the points that are the closest to a so-called *seed*, as shown in Figure 2.16. These regions are also known as *cells* and in this project they represent the main-phase $\beta - Sn$ grains.
Voronoi tessellations have been used extensively in computational material science to model random polygonal grains [39][40]. Currently, there is no readily available software for tessellating an arbitrarily-shaped 3D surface. Therefore, a script has been developed in Python for the task. The *scipy.spatial* library features a function named *Voronoi* capable of generating a Voronoi object starting from given seed coordinates. This function bases its outputs on the Voronoi *vertices*, i.e. the vertices of each cell polygon. The segments (in 2D) or planes (in 3D) connecting these vertices are known as *ridges*. Each ridge also corresponds to the boundary between two Voronoi cells.

Generating a Voronoi tessellation starting from completely random seeds may result in some cells having shapes that would be unrealistic for grains in a solder joint microstructure. One way to remedy this is by using *centroidal Voronoi tessellations*, in which every seed is also the centroid of its cell. This results in more regular cell shapes, as can be seen in Figure 2.17. A centroidal tessellation may only be achieved by having appropriate starting seeds. The *CVTSampling* function from the *idaes.surrogate.pysmo.sampling* library is capable of generating a random combination of such ”centroidal seeds”.

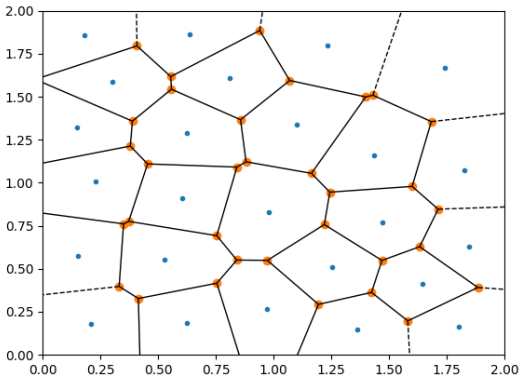

(a) 2D Centroidal Voronoi diagram from scipy.spatial.Voronoi. Seeds generated with idaes.surrogate.pysmo.sampling.CVTSampling

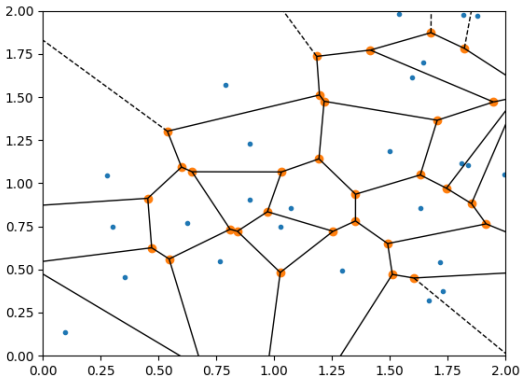

(b) 2D Non-centroidal Voronoi diagram from scipy.spatial.Voronoi. Note the irregular shape of some cells

Figure 2.17: Comparison between Centroidal and Non-centroidal Voronoi diagrams

As mentioned earlier, there is currently no software or Python library capable of bounding a

Voronoi diagram to an arbitrary 3D geometry. The diagrams generated by *scipy.spatial.Voronoi* are unbounded: the dashed lines in Figure 2.17 are unbounded ridges. For the purposes of this project, it is necessary to clip the unbounded ridges in the 3D Voronoi diagram into the truncated sphere shape typical of solder joints.

Voronoi Tessellation Script

The solder-shaped 3D Voronoi diagrams are generated through a combination of a Python script and a Marc script. Scripts in Marc are written using *py_mentat*, a Python library that comes with Marc capable of sending commands to the Marc graphical user interface. This split was done as some operations are performed more conveniently in Marc.

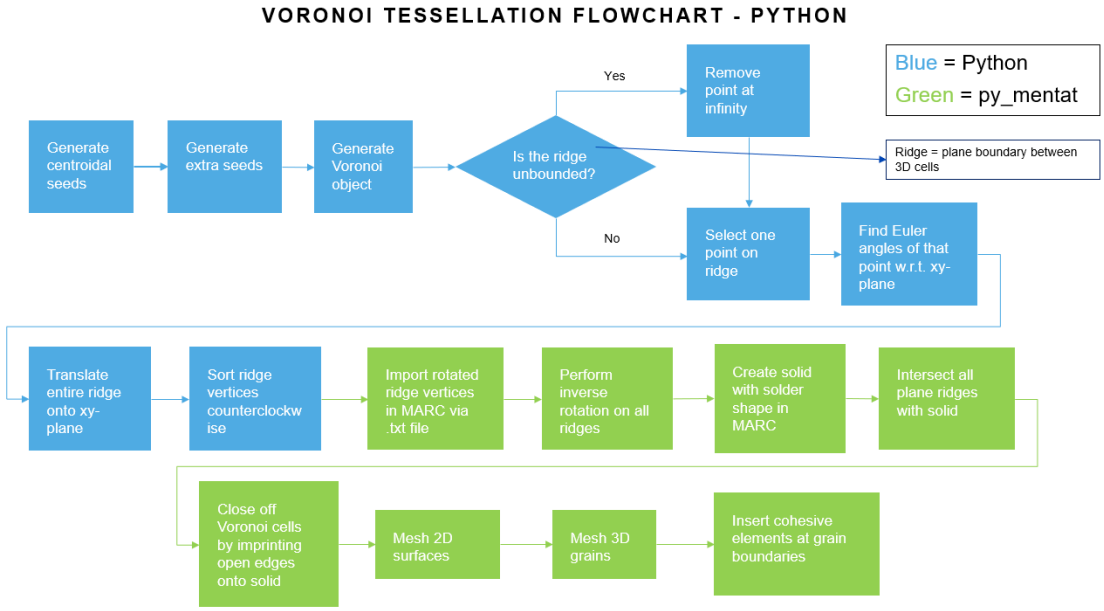

Figure 2.18: Flowchart of the Voronoi-generating script

The starting input of the script is the number of grains to be generated, which is chosen with the Python function *random.random* between 5 and 9. The Python script (the blue part of Figure 2.18) takes the number of seeds and generates the 3D centroidal Voronoi diagram. The diagram is pre-processed for Marc as a text file that documents the connectivity and vertex locations of each 2D surface, along with the two seeds it is associated to. This text file is then read by the *py_mentat* script, which uses the data to generate geometric solids (polygons) representing the grain boundaries. However, there is a caveat: the input Marc requires to create a geometric solid is the vertices of the solid provided in counter-clockwise direction. This is a problem when working with a 3D space as the concept of ”counter-clockwise” is meaningless in 3D. To circumvent this, the ridges were rotated onto the *xy*-plane and sorted counter-clockwise before being written to the text file and finally converted back to their original positions once they had been imported in Marc.

It was previously mentioned that the unbounded ridges generated by the Python script needed to be trimmed. This problem was solved by applying extra seeds at a significant distance from

the area where the solder joint is supposed to be. By doing so, the joint area is filled only with finite ridges since the unbounded ridges are now far from this area. The method is illustrated in Figure 2.19.

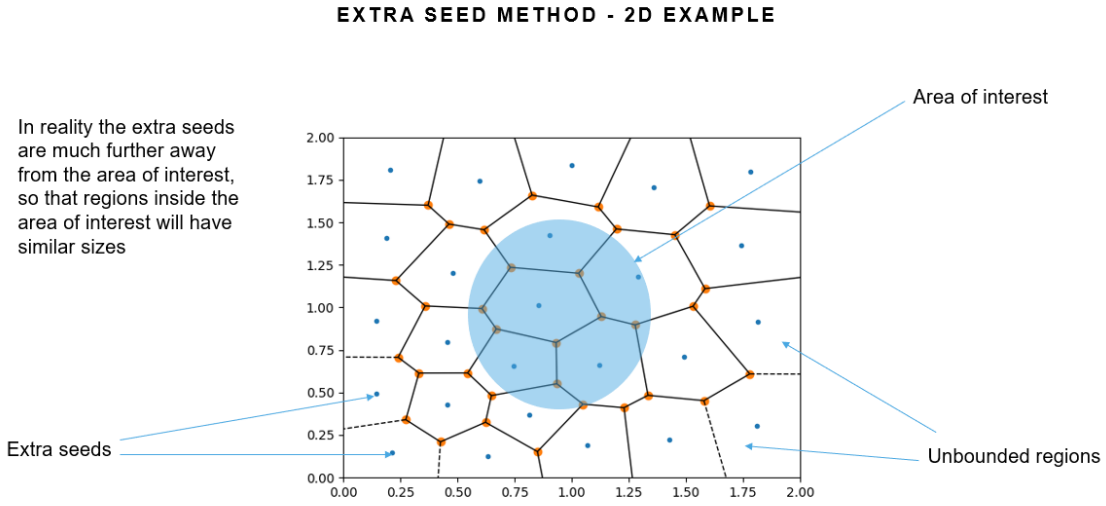

Figure 2.19: Illustration of extra seeds method for bounding of Voronoi region

The last step to obtain the microstructure geometry consists of intersecting the imported ridges with a solder joint-shaped solid. The far-off ridges that do not intersect the joint-shaped solid are automatically discarded. At this point, the joint-shaped solid is divided into grains by the intersected ridges as shown in Figure 2.20a. The geometry is then 3D meshed and fitted with interface elements at the grain boundaries (Figure 2.20b). The meshing process is explained in more detail in section 3.2.

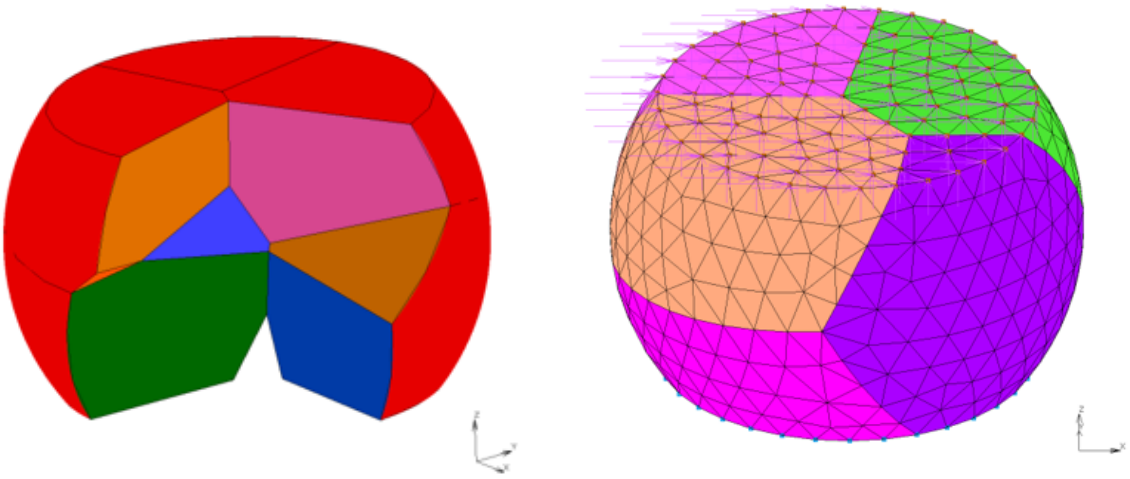

(a) Cross-section of geometric solids forming solder geometry

(b) Meshed solder geometry

Figure 2.20: Geometries of randomly-generated solder joints

3

Simulation Model of Single Solder Joint

This chapter and chapter 4 will focus on the implementation used to apply the theory described in chapter 2 to Marc Mentat. This chapter discusses the generation of the FE models used for the first two testing campaigns mentioned in section 1.1.

The following sections describe the settings used to create FE models of single solder joints that feature the microstructural characteristics introduced in chapter 2. The choices made during the pre-processing phase are explained and argumented in detail. Convergence studies on mesh size and increment time steps were also performed. Lastly, a previous experiment from the literature is recreated with the novel simulation approach introduced in this project for validation purposes.

3.1. Material Properties

The solder material used for this project is *SAC305*. The name contains details on the alloying components: *SnAgCu*, with 96.5% tin, **3**% silver , and **0.5**% copper. SAC305 is a common soldering metal for semiconductor packages. In addition to the anisotropic viscoplastic properties described by the Garofalo-Hill equations, the solder material exhibits anisotropic elasticity as well. To be accurate SAC305 is orthotropic, with two of the three principal directions having the same properties both for the elastic and the viscoplastic behavior. An approximation is made where the elastic constitutive matrix is constant with temperature, as the elastic properties of the *Sn*-majority SAC grains have not been yet well quantified over a range of temperatures [27]. The same applies to the Garofalo creep constants and the Hill coefficients. Thermal expansion is also enabled and is orthotropic in nature as well. The CTEs are linearly temperature-dependent. Overall, the material properties used for SAC305 are taken as used by Jiang et al. and references therein [27].

As mentioned earlier in section 2.4, the properties used for the isotropic grain boundaries are borrowed from the work of Jiang. These are the Young's modulus, the creep constant A_{GB} and Poisson's ratio. They are all temperature-independent as sufficient characterization is currently missing. Another important point to mention is that the grain boundaries do not feature thermal expansion; this could be a point of improvement for follow-up projects.

The copper used in the pads below and above the solder joints is approximated as a isotropic material with a constant CTE.

3.2. Meshing

The meshing process for the solder joint geometries is part of the script used to generate the solder joint geometries and as such it has been fully automated. A 2D mesh is first generated on the geometric solids produced by the Voronoi tessellation starting from surface seeds. The complete steps in the meshing process are:

- **Seeding of surfaces**: the solid surfaces are seeded according to the preferred seed size. This is the only input required by the script;
- **Surface Meshing**: a triangular 2D mesh is generated on the seeded solids;
- **Conversion of surface mesh to faceted surfaces**: faceted surfaces are unmeshed surfaces with a triangular facet pattern "imprinted" on them. The benefit of using faceted surfaces instead of a 2D mesh is that faceted surfaces are orientation-independent: it is not necessary for them to have normals oriented in the same direction (inside/outside);
- **Removal of geometric surfaces**: at this point the geometric solids are not necessary anymore and may be safely discarded;
- **3D Meshing**: a tetrahedron-based ("tet") 3D mesh is generated from the faceted surfaces using the default Marc mesher. Tets are used instead of hexahedron-shaped elements since they are better capable of reconstructing rounded shapes [41].

An overview of the process is depicted in Figure 3.1. The size of the elements in the figure is purely indicative; a more appropriate element size was determined via a mesh convergence study described later in section 3.7.

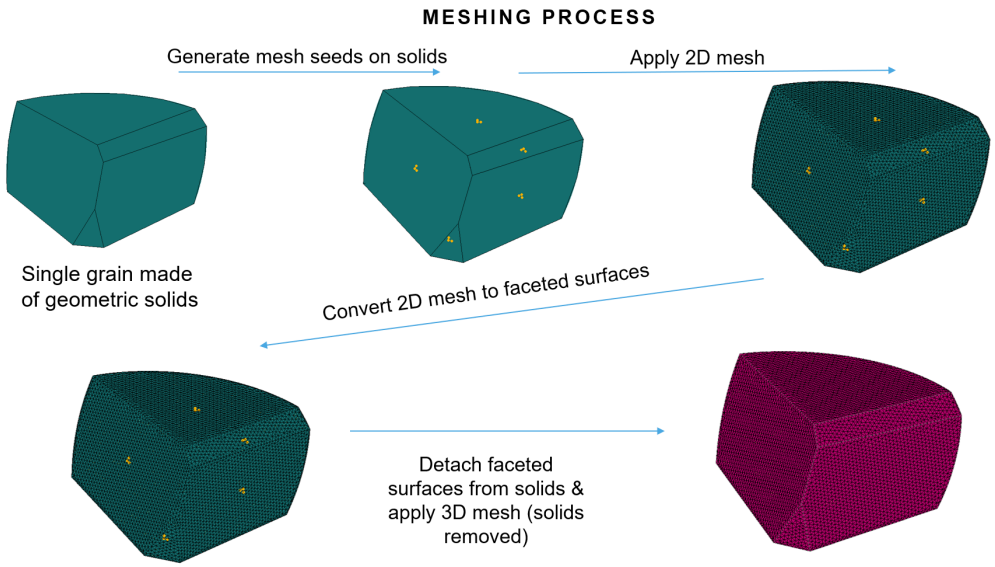

Figure 3.1: Example of 3D meshing process on a single grain

3.3. Boundary Conditions

The boundary conditions for the single solder joint models aim to simulate the loadcase of a solder joint embedded in a product undergoing thermal cycling. They are listed below and illustrated in Figure 3.2:

- Top pad: constant compressive load and cyclic horizontal shear load
- Bottom pad: whole pad constrained in z-direction, one point constrained in x- and y-directions and one point constrained in y-direction
- Temperature: cyclic profile (Figure 3.7) between -40°C and 125°C, 3 cycles starting from the stress-free temperature of 125°C.

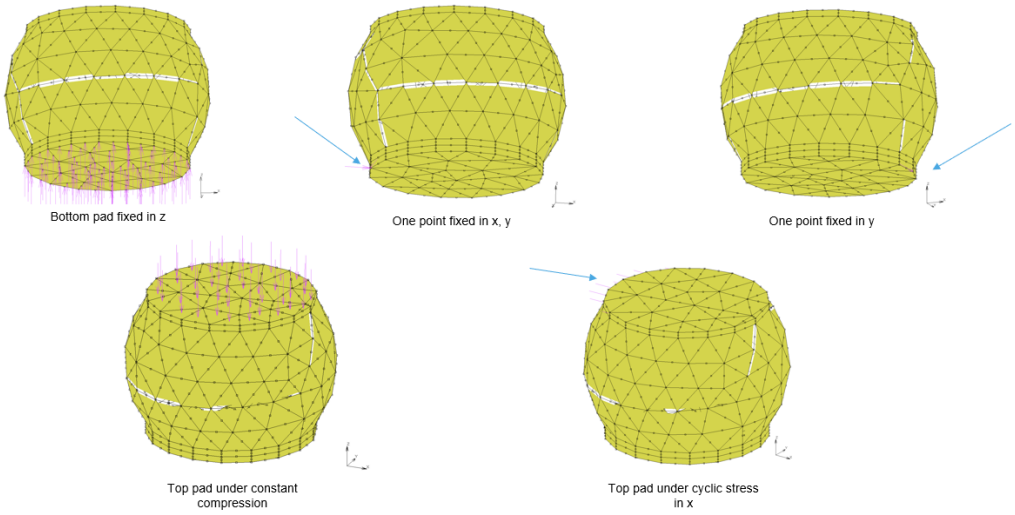

Figure 3.2: Boundary conditions for single solder models

The bottom pad is not fully clamped as that would prevent the thermal expansion of the pad and only contribute to generating internal stresses. The boundary conditions in Figure 3.2 allow the bottom pad to expand in the xy-plane.

3.4. Solder Joint Size

The size of all solder joints is constant and it has been chosen to be similar to solder joints currently used for Wafer-Level Chip-Scale Packages (WLCSP) and BGA packages developed by NXP. It is also consistent with the solder joints used in the literature experiment mentioned in section 3.9.

- Height (without copper pads): 175 μm
- Radius: 150 μm
- Top pad thickness: 8.75 μm
- Bottom pad thickness: 17.5 μm
- Pad radius: 125 μm

3.5. Extracting the Creep Strain Energy Density

The Creep Strain Energy Density (CSED) is a metric often correlated to fatigue damage in solder joints [33] [42]. It consists of the integral of the stress-creep strain curve:

$$\int_{\epsilon_0^{cr}}^{\epsilon_1^{cr}} \sigma d\epsilon^{cr} \tag{3.1}$$

In layman's terms, the CSED measures how much creep a material has undergone throughout its history. The CSED is an available output from Marc Mentat. In order to smooth out any

boundary effects, the CSED has been averaged over each grain and over the whole solder joint. To this purpose, a Python script was written. The script extracts the CSED values for each element and increment from the Marc output file, computes the average value for each grain/joint and then saves them in an Excel file. The results are then manipulated in Excel and Python.

3.6. Linear versus Quadratic Elements

The stress field resulting from the boundary conditions explained in section 3.3 is quite complex; as such, common linear elements might not be sufficiently accurate to model the solder behavior. The behavior of linear elements has been compared to that of quadratic elements in two different setups:

- A heavily simplified linear elastic analysis in which all sources of nonlinearity are removed (creep, nonlinear CTEs etc.);
- A fully nonlinear analysis.

The performance of linear and quadratic elements for the first setup is compared by means of a mesh convergence study shown in Figure 3.3. This convergence study was performed by using a constant solder geometry/orientation, changing exclusively the number of elements. The chosen output for this linear elastic simulations is the volume-averaged *Elastic Strain Energy Density*. It has been chosen because of its similarity to the desired output of the full simulations, which is the volume-averaged Creep Strain Energy Density.

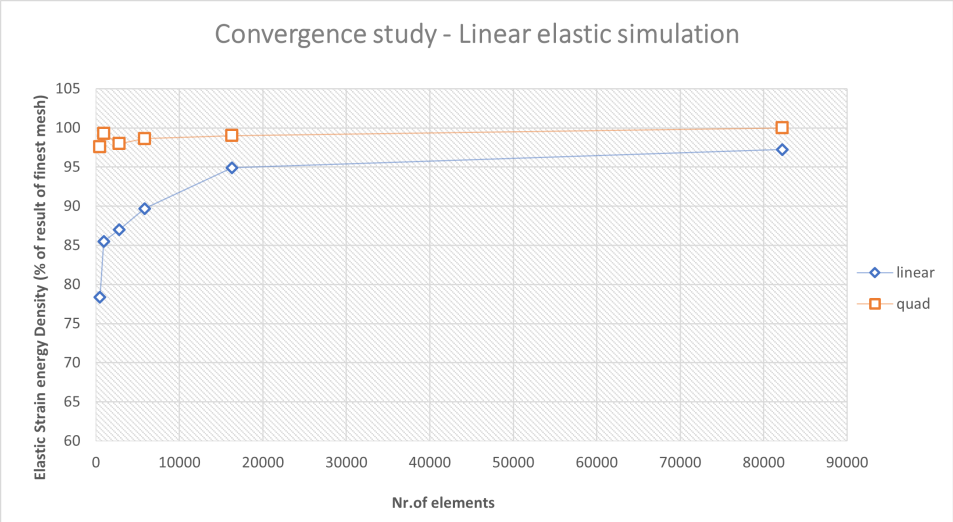

Figure 3.3: Behavior of linear vs quadratic elements in linear elastic simulation

It is evident that linear elements are much slower to converge than their quadratic counterparts. A follow-up mesh convergence study using the full non-linear model is performed in section 3.7.

3.7. Mesh Convergence

A mesh convergence study was performed on one solder joint with a constant microstructure in order to ensure a good combination of computational efficiency and accuracy before large amounts of simulations were run. A random solder was chosen; all non-mesh parameters such as grain orientations and time stepping criteria are kept constant in order to isolate the effect of the mesh. Both linear and quadratic elements are analyzed in this study, whose results are shown in Figure 3.4 and Table 3.1.

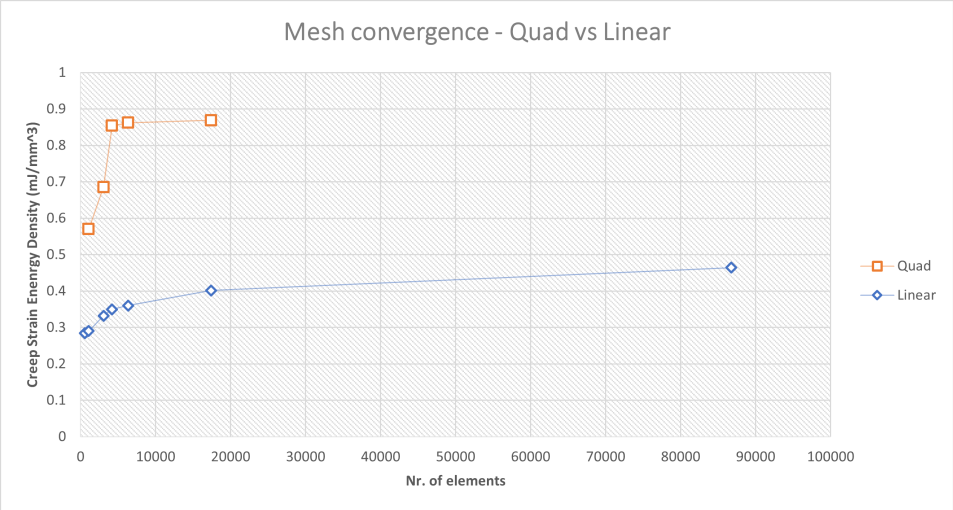

Figure 3.4: Mesh convergence comparison between linear and quadratic elements

Table 3.1: Mesh Convergence data points (quadratic elements)

Level of refinement (LOR)	1	2	3	4	5
Nr. of elements	1071	3071	4191	6337	17424
CSED (mJ/mm^3)	0.5701	0.68552	0.8538	0.8623	0.8688
% Δ w.r.t. finest mesh	34.37	21.09	1.72	0.74	0

Linear elements do not get close to converging even with almost 90,000 elements, further confirming that quadratic elements are necessary for the task. The ”level of refinement” (LOR) in Table 3.1 is associated to the surface mesh seed size used. An increasing level of refinement corresponds to a smaller mesh seed. LOR 3 already achieves results within 2% of those of LOR 5 despite having roughly a quarter of the elements. As such, LOR 3 is deemed converged and is used in all the following simulations.

3.8. Time Step Convergence

The influence of the increment time step Δt on FEM results is a well-known phenomenon. It is customary to check for convergence of results as the time step is reduced (leading to an increase in the number of increments). In the case of nonlinear material behavior, the time step size also affects the creep calculations: the integration schemes used to compute creep strains in section 2.3 and section 2.4 are dependent on Δt. Too large time steps might thus

lead to inaccurate results or even to non-convergence of the simulation. On the other hand, unnecessarily small time steps would increase computation effort beyond what is needed. A compromise has been found by performing a time step convergence study.

Given that hundreds of different solder geometries with different complexities have to be simulated, a fixed time step approach is not reasonable. A particular time step value might work for some solder joints but not for others. A more versatile approach is adaptive time stepping, in which the time step is modified during the simulation according to the current convergence status: if a particular increment converges quickly, the time step is increased on the next increment; if the opposite happens, the time step is made smaller.

The adaptive time stepping procedure is governed by a series of parameters shown in Figure 3.5. These values were decided according to trial-and-error and NXP know-how. The most important criterion is however not visible in Figure 3.5 (it appears in the ”User-Defined Criteria sub-menu”): the maximum time step allowed depends on the *maximum creep strain increment*. If the creep strain computed during an increment exceeds a certain value, the time step is decreased and the increment is restarted.

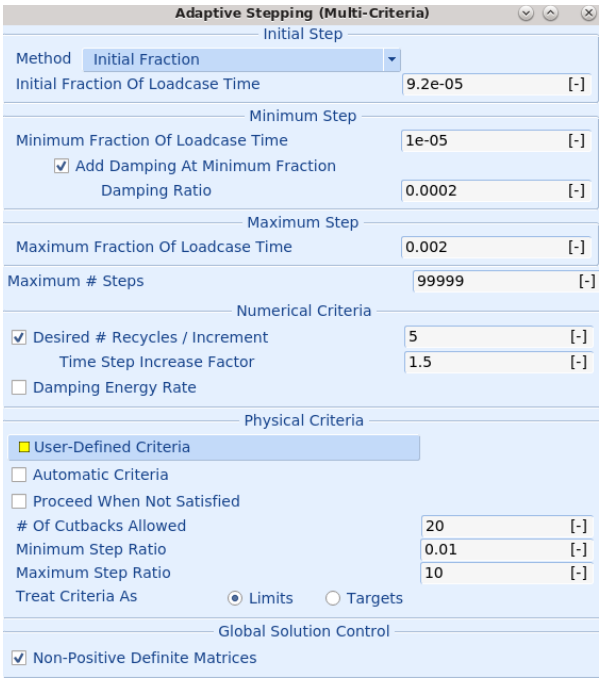

Figure 3.5: Overview of adaptive stepping criteria

The time step convergence study is thus performed in function of the maximum creep strain increment. One solder joint model is chosen (different from the one used in the mesh convergence study), the element size is kept constant (4191 elements, see section 3.7) and boundary conditions are implemented as described in section 3.3. The measured output is the volume-averaged CSED for the whole joint.

Table 3.2: Time step convergence data points

	1	2	3	4	5
Max creep strain inc (-)	7.05E-4	5E-4	2.5E-4	5E-5	1E-5
CSED (mJ/mm^3)	not converged	0.5783	0.5778	0.5766	0.5701
Run time (s)	-	266.13	268.55	505.82	2435.42
Nr. of increments	-	642	660	1178	5622

Some maximum creep strain increment values higher than 7.05E-4 were also tested but none of them converged. Table 3.2 shows that all converged models yield similar results, with the run time increasing sharply for maximum creep strain increments smaller than 5E-5. Even though a maximum creep strain increment of 5E-4 already provides accurate results, 5E-5 was chosen for the rest of the simulations in order to improve the chances that all simulations will run successfully.

3.9. Validation: Replication of Previous Experiment

A relevant experiment involving anisotropic grain-scale modeling of solder joints was performed by Hauck et. al [35] in which the 3-grained solder joint shown in Figure 4.7a was fitted with the Garofalo-Hill constitutive model. The solder used in this experiment does not feature cohesive elements at the grain boundaries, rather the grain boundaries are modeled as thin single layers of solid elements equipped with the same constitutive model as the one described in section 2.4. A critical grain orientation has been analyzed.

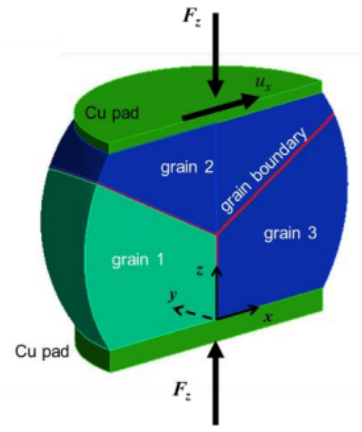

(a) 3-grained solder joint model from [35]

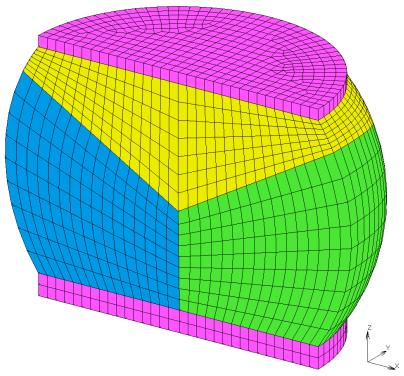

(b) Replica of solder joint from [35]. Invisible interface elements have been placed between the grains

Figure 3.6: Comparison of 3-grained solder models

The geometry has been recreated in Marc Mentat and used as a means to validate the implementation of the material constitutive models for both grains and grain boundaries. The boundary conditions have been kindly provided by the authors and are:

- A constant compressive stress of 0.1 MPa on the top pad;

- A cyclic shear displacement applied on the top pad in the x direction. The loading profile is given in Figure 3.7. For convenience the recreated simulation only uses the first three hours;
- The bottom pad is fully constrained in all directions;
- A cyclic temperature profile as shown in Figure 3.7. Again, only the first three hours are used;
- A symmetry constraint over the cross-section.

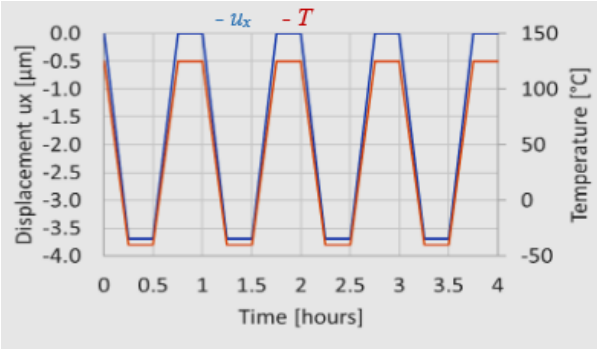

Figure 3.7: Temperature and displacement profiles from [35]

The simulation results to be compared are the volume-averaged accumulated creep strain energy densities for each of the three grains. The chosen grain material orientation is the orientation found to generate the highest creep magnitude in the bottom-left grain. In Hauck's study, the grain orientations are expressed in terms of the axis aligned with the principal material direction (the local z-axis). For instance, "yyz" means that in grains 1 and 2 the local z-axis is aligned with the global y-axis while in grain 3 the local and global coordinate systems coincide (local z-axis aligned with global z-axis). The constitutive thickness of the interface elements has been set to be equal to that of the literature model.

Table 3.3: Comparison between models for yyz configuration

Model	CSED Grain 1 (mJ/mm^3)	CSED Grain 2 (mJ/mm^3)	CSED Grain 3 (mJ/mm^3)
Hauck et al.	1.2356	0.2053	1.1229
This thesis	1.2006	0.2293	1.1165

The comparison between the two models yields satisfying results. Other than the inherent difference between solid element boundaries and interface element boundaries there are some factors that might explain the small difference in calculated results:

- The boundaries in the literature model feature a coefficient of thermal expansion while the cohesive boundaries do not;
- The mesh is slightly different between the two models due to the removal of the solid elements at the boundaries;

- The time stepping procedure of the literature model is unknown and likely different from the one used in Marc.

The results of this validation process show that interface elements can be used to model grain boundaries.

4

Simulation Model of Sample Product

The last part of the project consists of combining multiple solder joints into a simplified product model (Figure 4.1). The model represents a Ball-Grid Array (BGA) package that is connected to a PCB through nine solder joints. A pool of 100 unique solder joints was generated according to the methodology described in chapter 3; the nine solder joints used in each sample product were chosen at random from this pool.

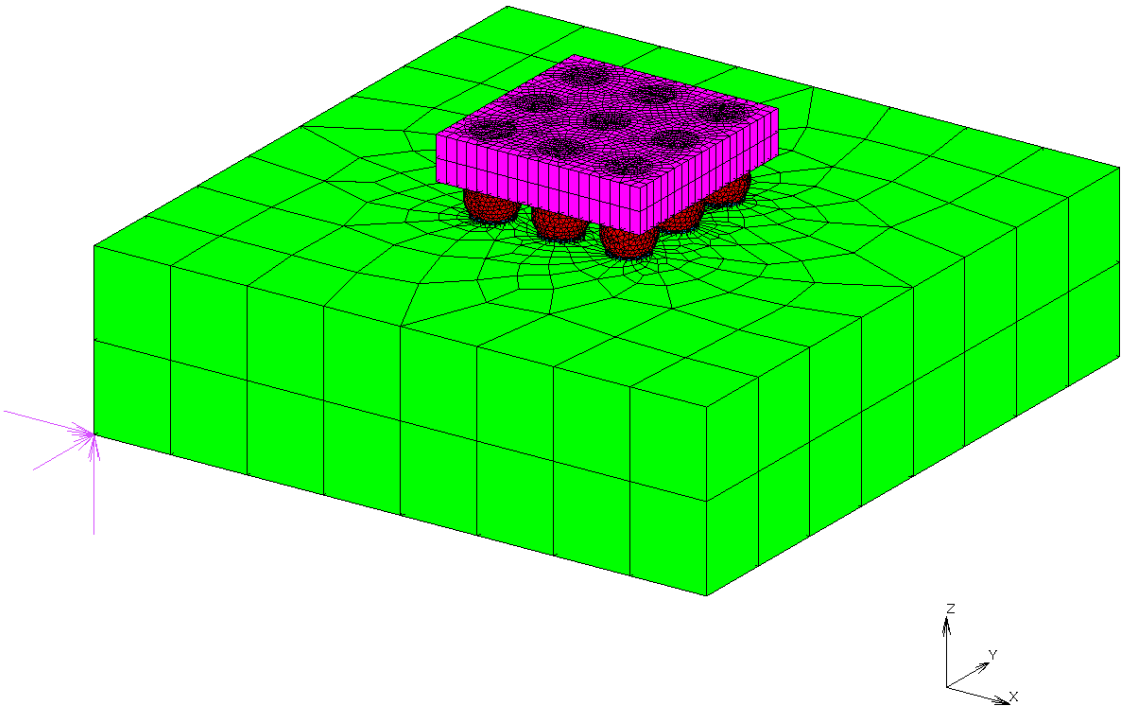

Figure 4.1: FEM model of sample BGA product

The sample product has been designed according to NXP expertise. The silicon die (in pink in Figure 4.1) is approximated as a uniform block of silicon, while the PCB (in green) is made of FR-4, a glass-reinforced epoxy laminate material.

4.1. Material Properties

The silicon is treated as an isotropic material with E = 169 GPa and ν = 0.23. The CTE is defined as temperature-dependent (2.35*10^{-6} 1/°K at room temperature). The PCB is also treated as an isotropic material, but in this case E is temperature dependent (17.4 GPa at room temperature) while the CTE is constant at 1.96*10^{-5} 1/°K.

4.2. Meshing

The solder joints are imported directly as they are. Since the solder joints feature quadratic elements, all the other components of the sample product must be made of quadratic elements as well. Linear and quadratic elements cannot be easily connected: the additional nodes present in a quadratic element would not be connected to a corresponding node in a linear element, leading to undesired phenomena such as interpenetration. The most direct way to avoid this problem is to exclusively use quadratic elements.

However, quadratic elements are more computationally expensive than their linear counterparts. In order to reduce the total amount of elements, the PCB has been fitted with a variable-size mesh. As the PCB is a simple shape with uniform material properties, coarser elements may be used to model it. The elements become smaller and smaller in proximity of the solder joints in order to ensure continuity with the finer mesh of the copper pads. The mesh around the copper pad area is highlighted in Figure 4.2. The mesh for the silicon is chosen to have a slightly larger seed size than the solder joints. The meshes were first generated on 2D planes in contact with the copper pads and then extruded in the vertical direction.

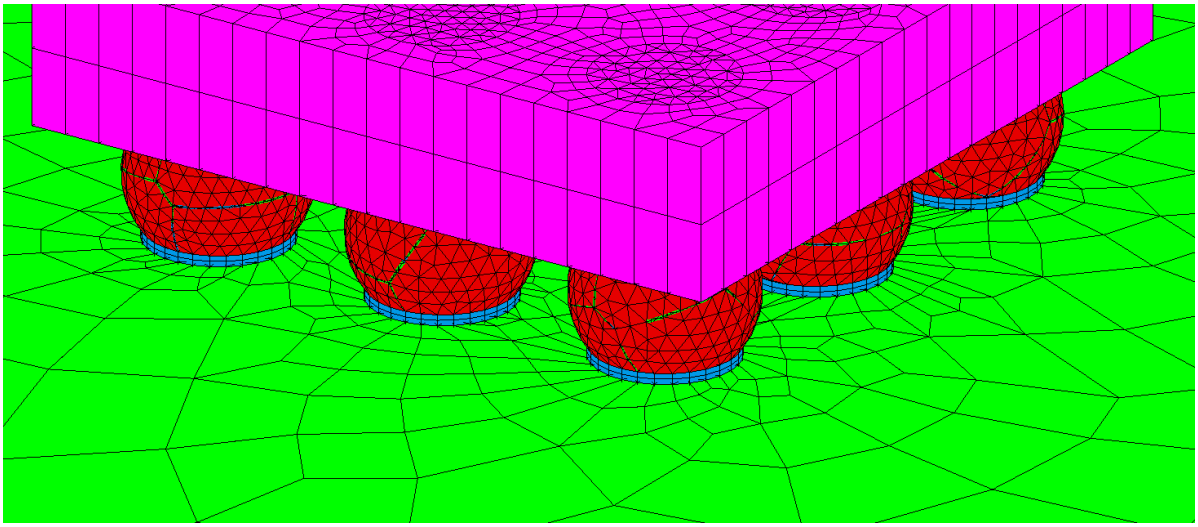

Figure 4.2: Highlight of mesh around the copper pad area

4.3. Boundary Conditions

The boundary conditions for the sample product model differ from that of a single solder. In the single solder, the imposed stresses are used to simulate the effect of the CTE mismatch between solder joints, PCB and silicon. Since the sample product explicitly features the PCB and the silicon, these imposed stress conditions are not necessary: the only applied loading is the temperature cycling. To summarize:

- Bottom of PCB: one point fixed in x-,y- and z-directions, one point fixed in y- and z-directions and one point fixed in z-direction. These boundary conditions prevent in- and out-of plane rotations while leaving the free surfaces such as the bottom of the PCB and the top of the silicon free to expand and contract;
- Temperature: cyclic profile (Figure 3.7) between -40°C and 125°C, 3 cycles starting from the stress-free temperature of 125°C.

4.4. Extracting the Creep Strain Energy Density

The process used to extract the CSED is analogous to that used in the study of single solder joints. Again, the CSED in the solder joints is extracted by means of a Python script and averaged over the volume of the individual grains as well as the whole solder joints.

5

Results & Discussions

This chapter presents the findings of the three simulation campaigns mentioned in section 1.1. The main output variable of the FEM simulations for the three campaigns is the volume-averaged CSED accumulated over the thermal cycling process. The CSED has been averaged over different volume domains in order to provide more insight on the behavior of individual grains and of solder joints as a whole. In section 3.5 it was explained that the CSED has been often related to fatigue damage in solder joint reliability literature. As such, a postulate is made that the fatigue life of a solder joint or grain is inversely proportional to the volume-averaged accumulated CSED. The purpose of this postulate is to bridge the gap between simulation results and real-life fatigue endurance.
When relevant, comparisons with real reliability data were made. The focus of these comparisons is not an accurate prediction of the cycles to failure but rather the characteristics of the data point distributions.

5.1. Effect of Grain Orientation on Single Solder Joint

The first simulation campaign had the objective of testing 100 solder joints with a fixed-grain microstructure and constant boundary conditions, with the only variable being the material orientation of the grains. The specific solder joint geometry used for this campaign is shown in Figure 5.1. This joint features 5 grains, which is the minimum among the solder joints used in this project. This choice was made to maximize the effect of the orientation of each grain on the behavior of the whole solder joint.

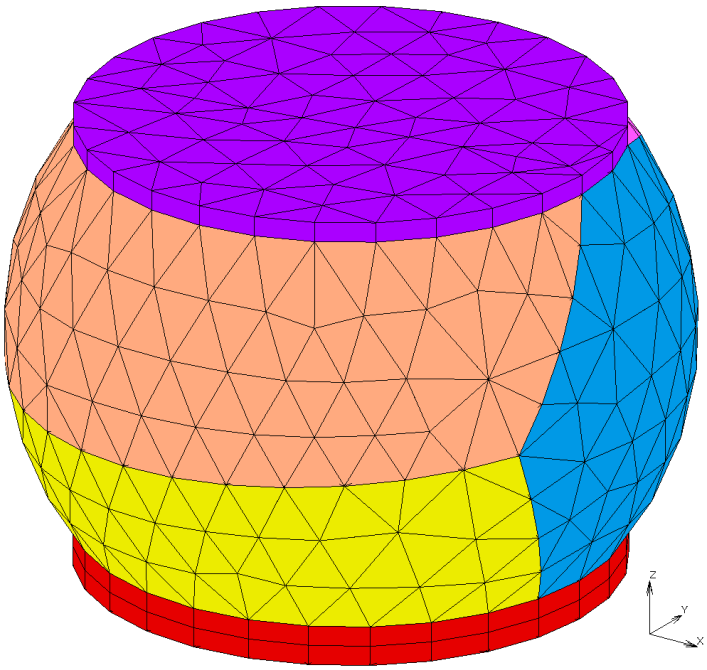

Figure 5.1: Solder joint used for first simulation campaign

First, the average CSED over the whole solder joint is analyzed for the 100 different combinations of grain orientations. The distribution of CSED values is shown in Figure 5.2.

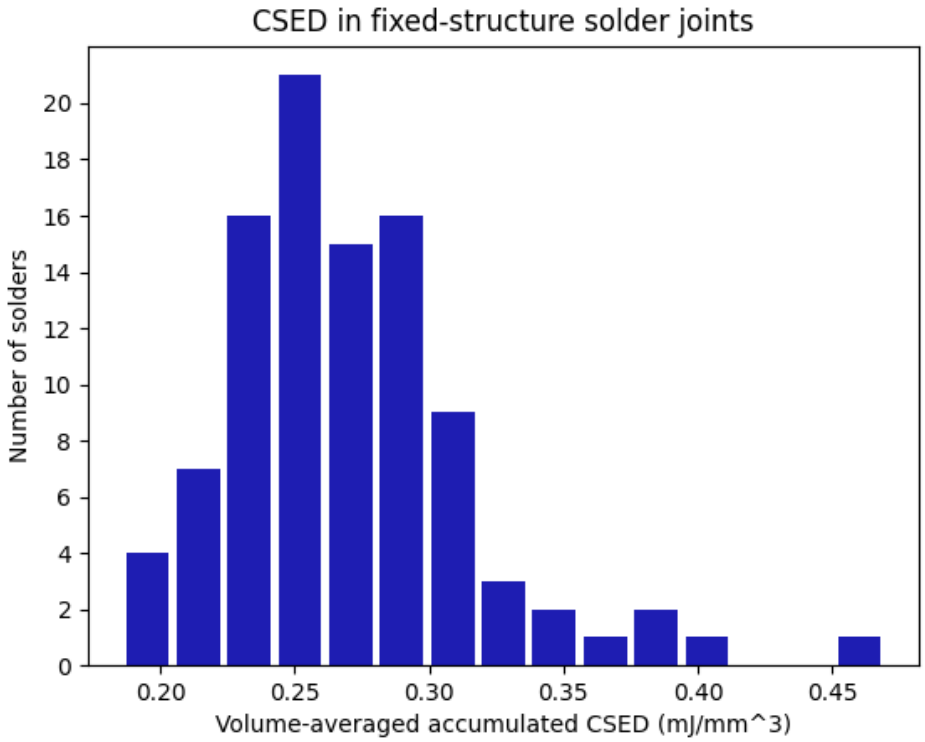

Figure 5.2: Histogram of CSED of solder joints with fixed-grain structure

The solder joint with the most creep-sensitive grain orientations experiences approximately 2.5 times as much accumulated CSED than the least sensitive one.

The CSED is then calculated and averaged over the volume of each grain. It is particularly useful to look at the grain that accumulates the highest CSED within a solder joint (referred from now on as ”most critical grain”). As the fatigue life of the solder material is assumed to be inversely related to CSED, an eventual fatigue crack is expected to nucleate in proximity of this most critical grain. In order to estimate the fatigue life N_f of each solder joint, an arbitrary constant of proportionality was chosen and divided by the accumulated CSED:

$$N_f = 3000/CSED \tag{5.1}$$

The 2-parameter Weibull distribution has been chosen for a qualitative statistical analysis of the amount of thermal cycles to failure for the solder joints. The Weibull distribution is used extensively in reliability engineering to model lifetime distributions [43]. One of its main advantages is its versatility: by changing the shape parameter β, the Weibull distribution can take on the characteristics of other types of distributions. The other Weibull parameter α is known as the *characteristic life*, which is the number of cycles at which 63.2% of the samples have failed [44]. β on the other hand is used as a measure of the uniformity of the sample points used in the distribution. When the dataset is made into a log-log probability plot such as the one in Figure 5.3, β corresponds to the slope of the fit. A higher slope means that the product failures are closer in time to each other. The constant of proportionality used in Equation 5.1 affects α but not β. A change in α has no effect on the statistical properties of the distribution as all data points would be shifted along the x-axis of the log-log probability plot by the same amount. Figure 5.3 presents the probability plot of the Weibull distribution of grains with the highest CSED for each solder joint. The blue-shaded region represents the 95% confidence interval.

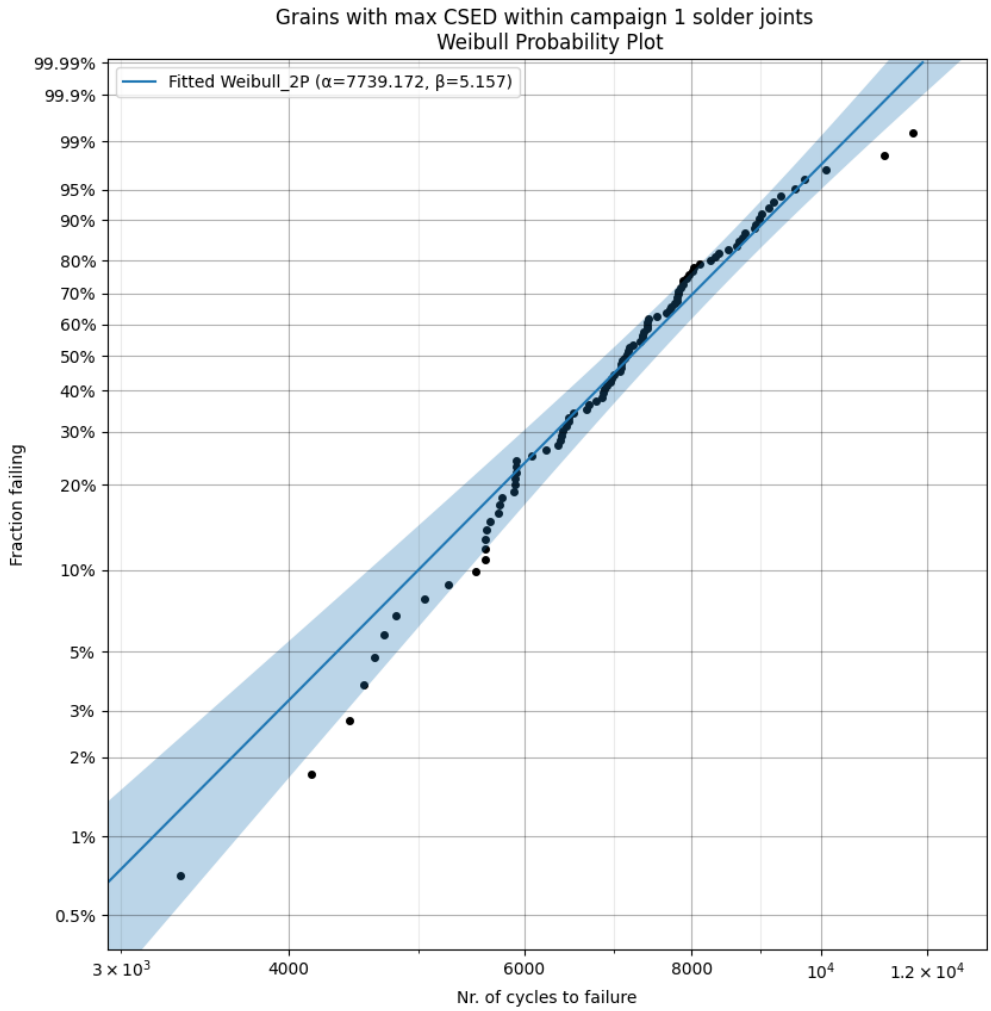

Figure 5.3: Weibull probability plot of most critical grains in each solder joint used in campaign 1

The latest failure happens at a number of cycles ≈ 3.5 times higher than the first failure. The relevance of the β parameter in the fit shown in Figure 5.3 is explained later in a comparison with analogous results from the second simulation campaign.

5.2. Effect of Combined Microstructure Parameters on Single Solder

The second simulation campaign expanded on the first one: now each solder joint has a unique microstructural geometry, where the orientation of each grain is randomized as well. Again, 100 unique solder joints were simulated. The boundary conditions are again the same for all the joints. The CSED is first extracted and averaged over the whole solder joint volume; the resulting distribution is shown in Figure 5.4.

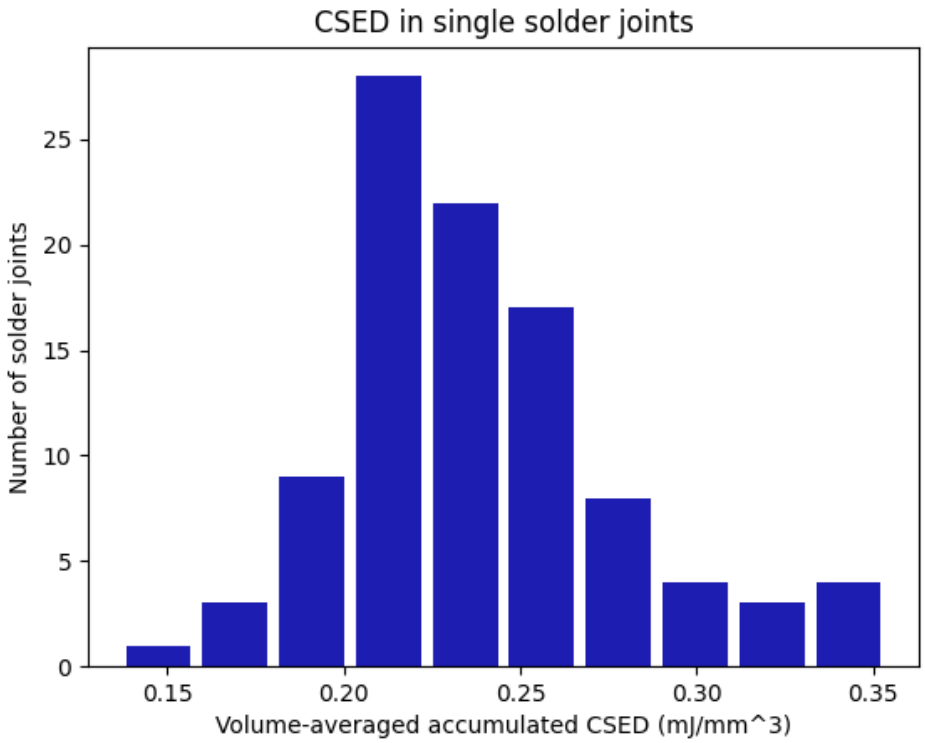

Figure 5.4: Histogram of CSED of solder joints with variable microstructural geometry

With respect to the results from the first simulation campaign (Figure 5.2), the difference between the lowest and highest accumulated CSED values is similar at about 0.20 mJ/mm^3. This suggests that the material orientations of the grains have a more significant effect on the resulting variability than the shape and amount of grains.
While the variability seems to be unaffected, the magnitude of the accumulated CSED is influenced by the grain geometry. The mean for the CSED values in Figure 5.4 is lower than that of the data in Figure 5.2 (0.2378 vs 0.2702 mJ/mm^3 respectively): this shows that the grain geometry in the solder joint used for the first simulation campaign was particularly sensitive to creep. An interesting insight from Figure 5.4 is the difference in CSED between the most and least creep-sensitive joints. The least creep-sensitive solder joint experiences an accumulated CSED 0.137 mJ/mm^3 while the most sensitive one accumulates 0.354 mJ/mm^3: more than 2.5 times as much.

Similarly to the first campaign, the CSED was also averaged over the volume of the individual grains and again the most critical grain in each solder joint was considered for a Weibull failure distribution. The corresponding probability plot is presented in Figure 5.5.

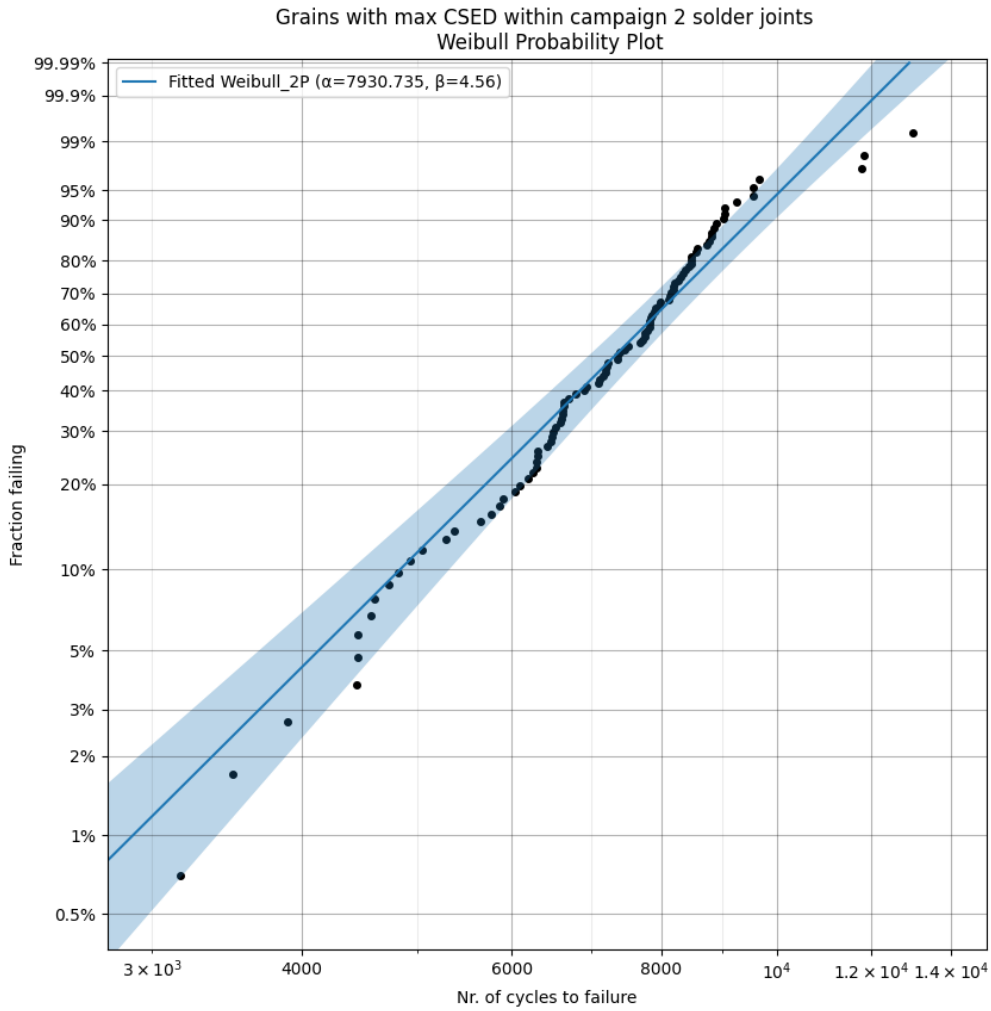

Figure 5.5: Weibull probability plot of most critical grains in each solder joint used in campaign 1

The higher microstructural variability of the solder joints from campaign 2 with respect to those from campaign 1 is reflected in the Weibull probability plots. The fit in Figure 5.5 has a lower β than that of Figure 5.3 (4.56 vs. 5.16, respectively), meaning that the failures are spread over a wider range of cycles and the data has a higher variability. The higher microstructural variability of the joints also shows in the ratio between last and first failure. This is higher for the second campaign ($\approx$ 4.1) than the first campaign.

Effect of number of grains within solder joint

An additional analysis was performed on the results of the second simulation campaign to investigate whether the number of grains in a solder joint is correlated to the overall creep response of the whole joint. To this end, the CSED data for the whole solder joints from Figure 5.4 has been sorted by number of grains in the joint. This sorted data is shown in the form of box plots in Figure 5.6. It seems that the number of grains in a joint does not have a significant effect on neither the magnitude nor the variance of the CSED that developed within the solder joints.

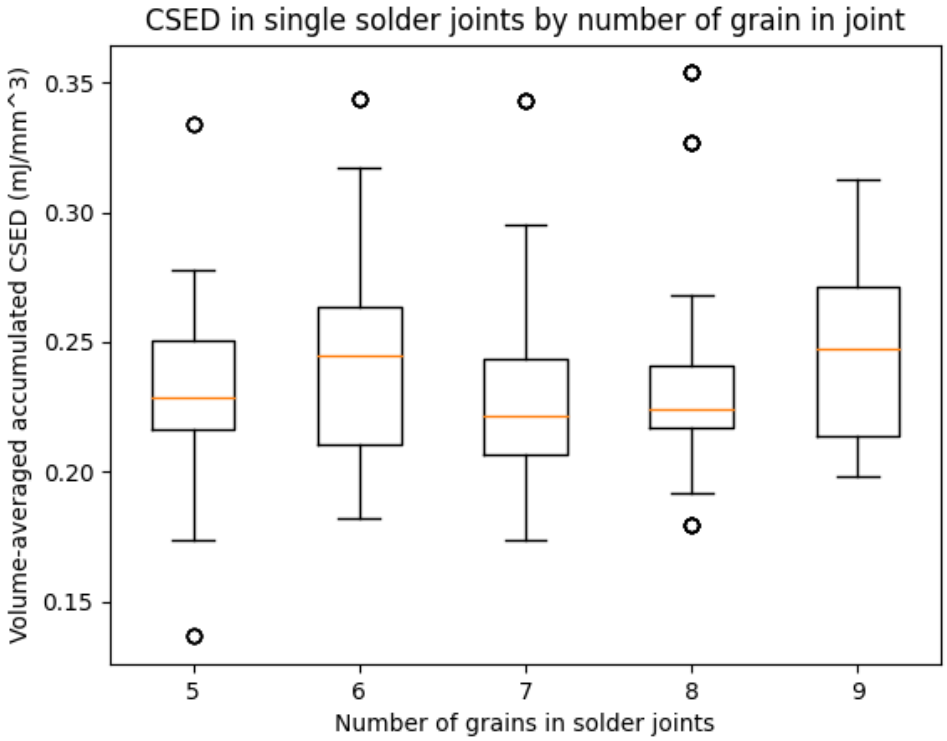

Figure 5.6: Box plot of CSED in single solder joints sorted by number of grains in the joint

5.3. General Behavior of Sample Products

Before the results of the third and final simulation campaign are presented, some observations about the general behavior of solder joints within the sample products are discussed. Figure 5.7, Figure 5.8 and Figure 5.9 show the cross-sections of three solder joints taken from one sample product after one, two and three thermal cycles respectively. The CSED accumulates initially at the corners and later spreads along the interfaces with the copper pads. As the CSED is correlated with fatigue damage, it may be inferred that an eventual crack would begin at the corners and then propagate along the interface. This behavior is in accordance with numerous studies on the thermomechanical response of SAC solder joints [34] [45] [46].

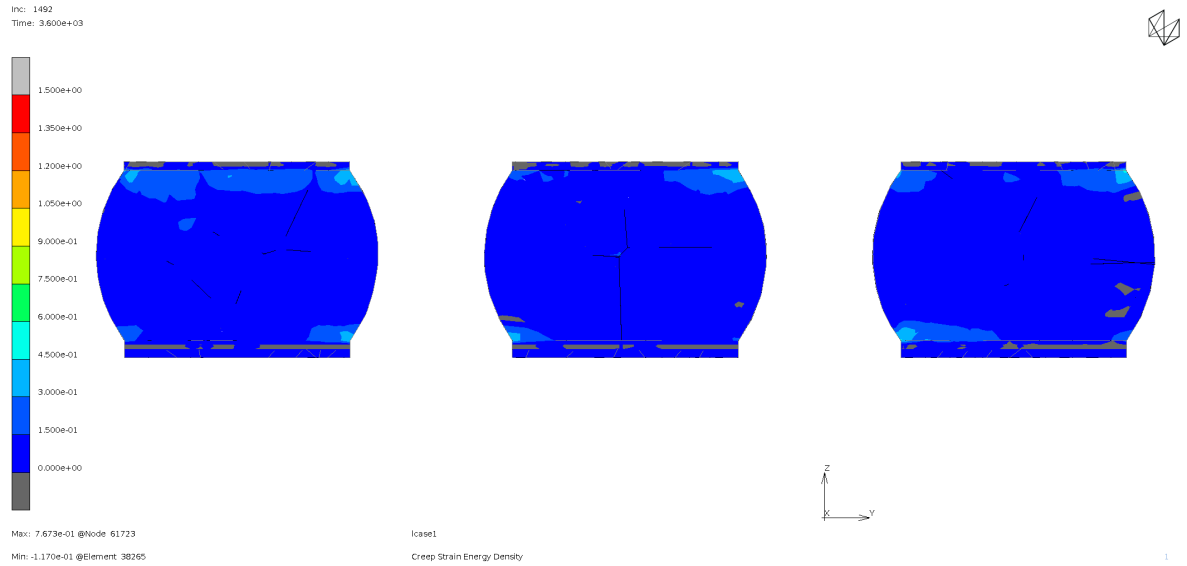

Figure 5.7: Cross Section of 3 solder joints from sample product after one thermal cycle

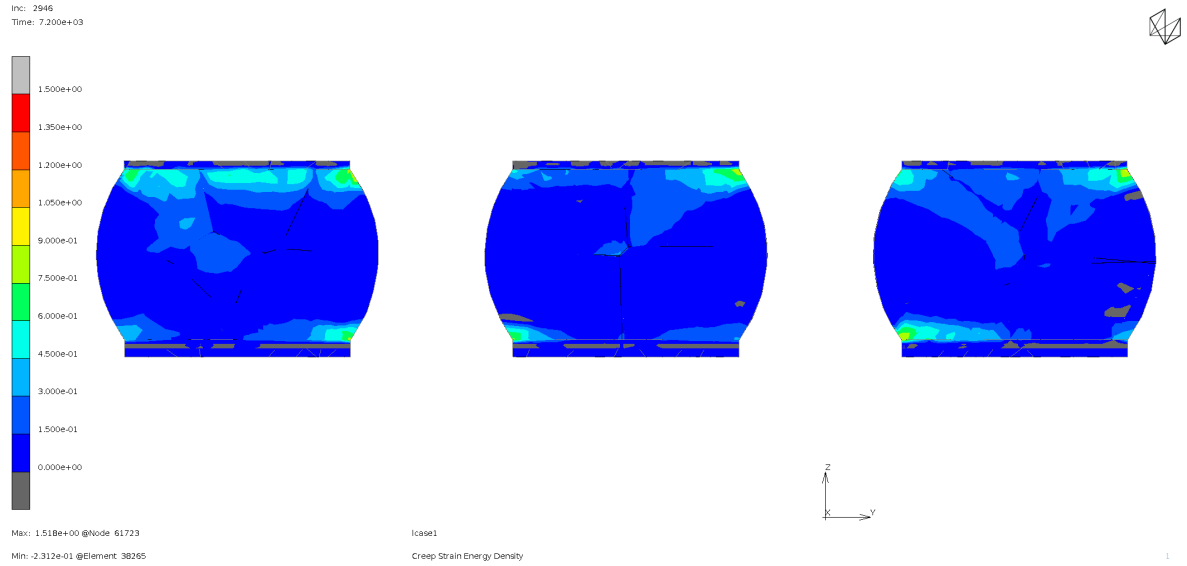

Figure 5.8: Cross Section of 3 solder joints from sample product after two thermal cycles

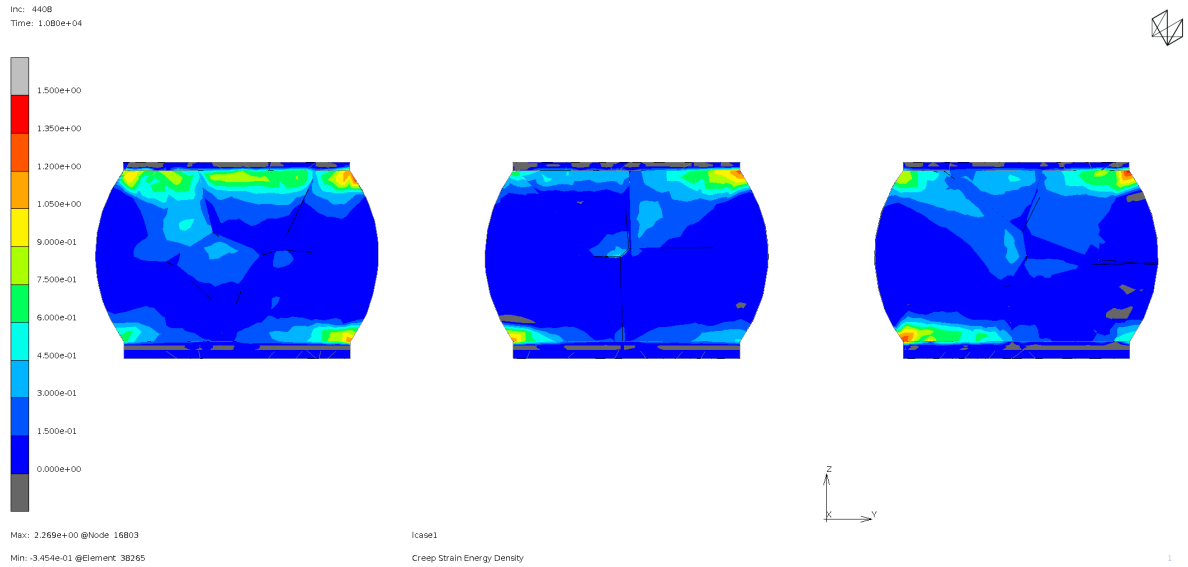

Figure 5.9: Cross Section of 3 solder joints from sample product after three thermal cycles

Figure 5.10 depicts the CSED in the solder joints from one sample product after three thermal cycles. The joints at the corners experience higher CSED magnitudes. The explanation for this is their increased distance from the assembly's neutral point: with all components expanding and contracting radially due to temperature, the central solder joint will experience the smallest mismatch in displacement while the furthest solder joints will experience the highest mismatch.

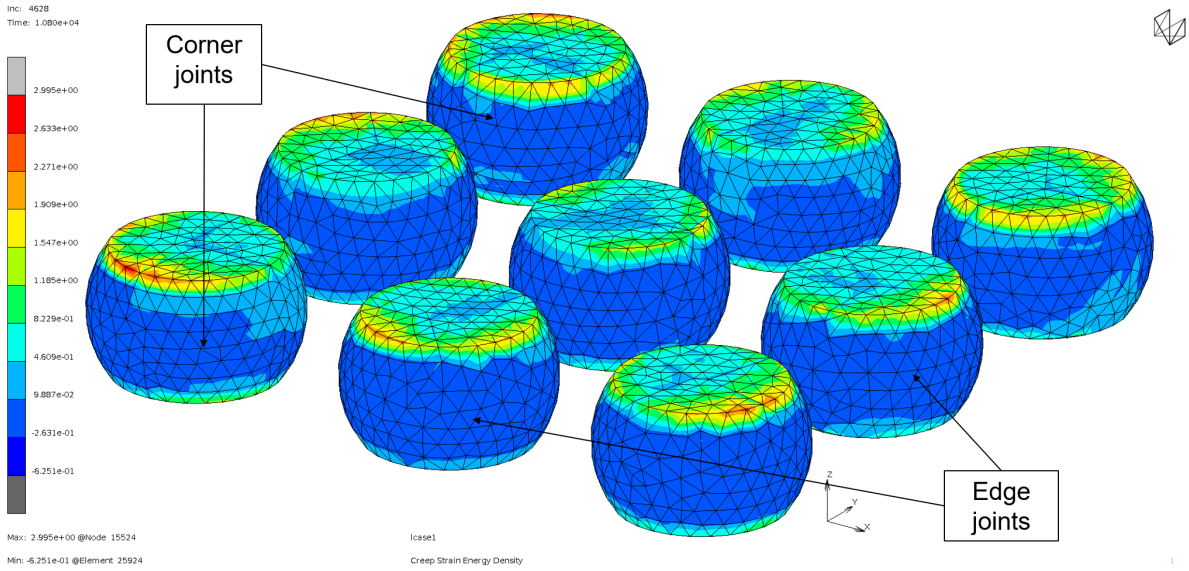

Figure 5.10: Overview of CSED in solder joints from sample product

5.4. Stochastic Analysis of Solder Joints Embedded in the Sample Product

For the third simulation campaign, 34 sample products were simulated, each fitted with a unique combination of random solder joints. The statistical analysis of the dataset obtained from this campaign was performed similarly to that of the first two campaigns. The accumulated CSED has been averaged over the volume of the solder joints and the volume of the grains. On a solder joint level, there is now a key difference with the first two simulation campaigns: section 5.3 mentioned that the magnitude of CSED accumulated in a joint is dependent on the joint's location within the product. The first analysis of this section has the objective of assessing the influence of the joint's location within the product and comparing it with the influence of variations in microstructure. Figure 5.11 shows the CSED averaged over the solder joint volume for the corner and edge joints in all the products. Here, "edge" refers to all solder joints at the edge of the solder joint array minus the corner ones (see Figure 5.10).

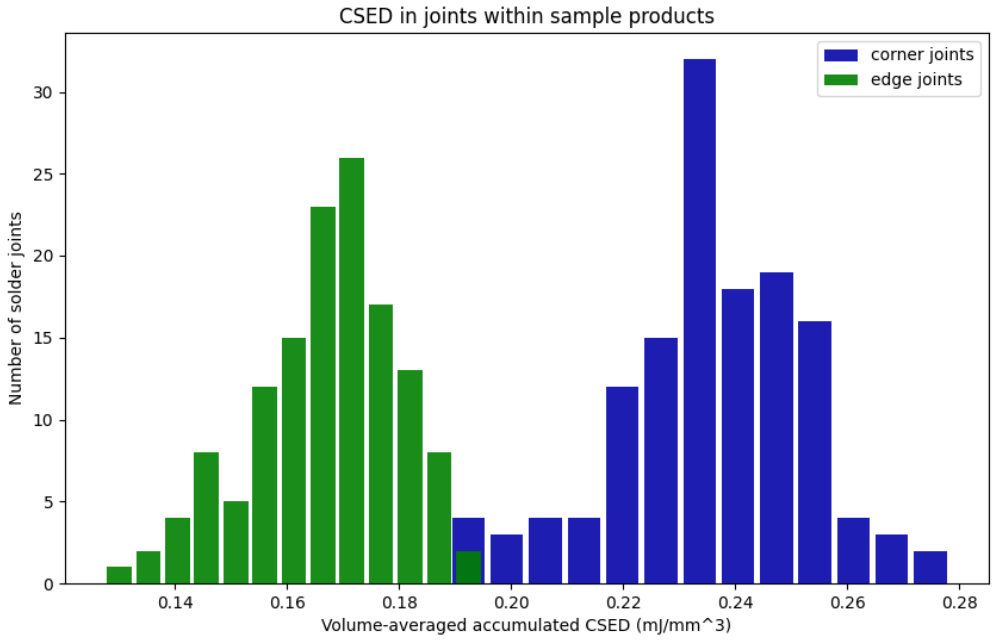

Figure 5.11: Histogram of CSED of corner and edge joints from sample products

Table 5.1: CSED comparison between edge and corner solder joints for campaign 3

Dataset	Corner joints	Edge Joints
Maximum (mJ/mm^3)	0.278	0.195
Minimum (mJ/mm^3)	0.189	0.128

The distributions for the edge and corner datasets are qualitatively similar. The most noteworthy observation is that the highest CSED value in the edge joint dataset is higher

than the lowest value from the corner dataset. This does not necessarily mean that a sample product may have its most critical location w.r.t. solder fatigue outside of a corner joint, as the maximum edge joint CSED and the minimum corner joint CSED are coming from two different sample products.

Critical sample product

A special sample product was tested to verify whether an edge joint could accumulate more CSED than the corner joints due to having a particular microstructure. Bieler et al. [5] stated that the most critical $\beta - Sn$ orientation with respect to fatigue fracture is the one in which the material z-axis is parallel to the PCB. It is then hypothesized that the most creep-resistant orientation is that in which the material z-axis is perpendicular to the PCB. In this special sample product, the edge joints were fitted with the most critical orientation while the corner joints had the least critical orientation. The extracted CSED for each solder joint in this sample product is visualized as a bubble plot (in which each bubble represents a solder joint) in Figure 5.12:

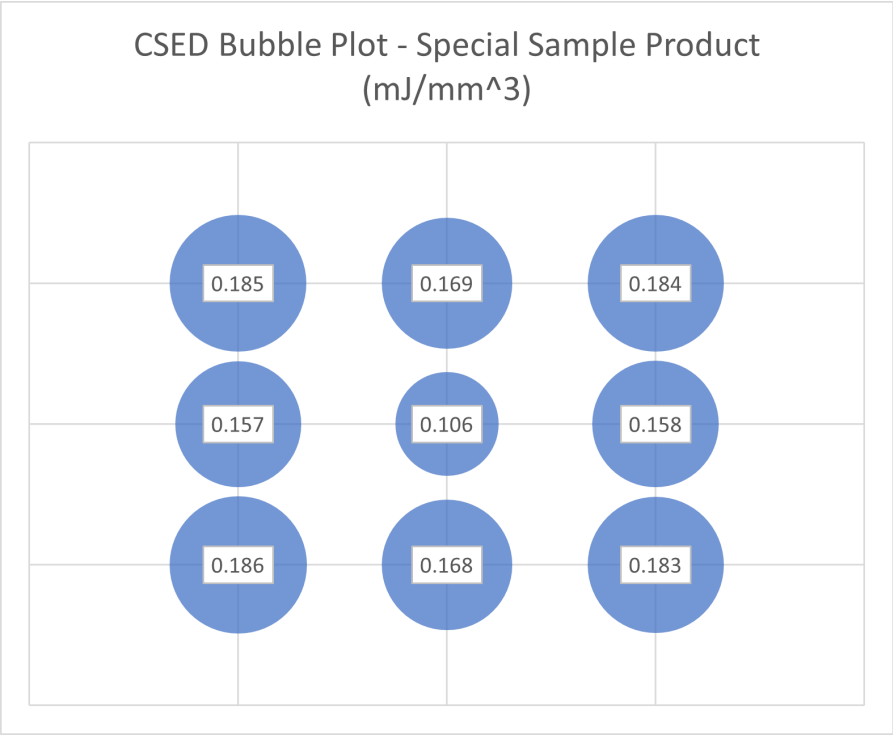

Figure 5.12: Bubble plot representing the accumulated CSED in each joint of the special sample product

It can be noted that the CSED values for the edge joints do not exceed those of the corner joints. Thus, a solder joint's location within the package as a higher influence on its creep response than its microstructure. This observation might however not hold up for larger solder joint arrays. In the current 3x3 setup, difference in relative distance from the neutral point between adjacent joints is significant. WLSCP packages typically feature solder joint arrays with between 2 and 12 solder joints per side [47]. For a larger array, this difference would become smaller in adjacent joints. Therefore, the effect of the solder joint's location within

the array should diminish. As a consequence, the effect of the microstructure on the creep response might become dominant over the effect of location.

Distribution of CSED for grains in sample products

The distribution of CSED for the grains within the sample products is arguably the most useful result in this chapter for comparison with real-life reliability testing, especially when the most critical grains from each sample product are considered.
Figure 5.13 shows the probability plot of the distribution of grains with highest CSED for each sample product. The blue-shaded region represents the 95% confidence interval.

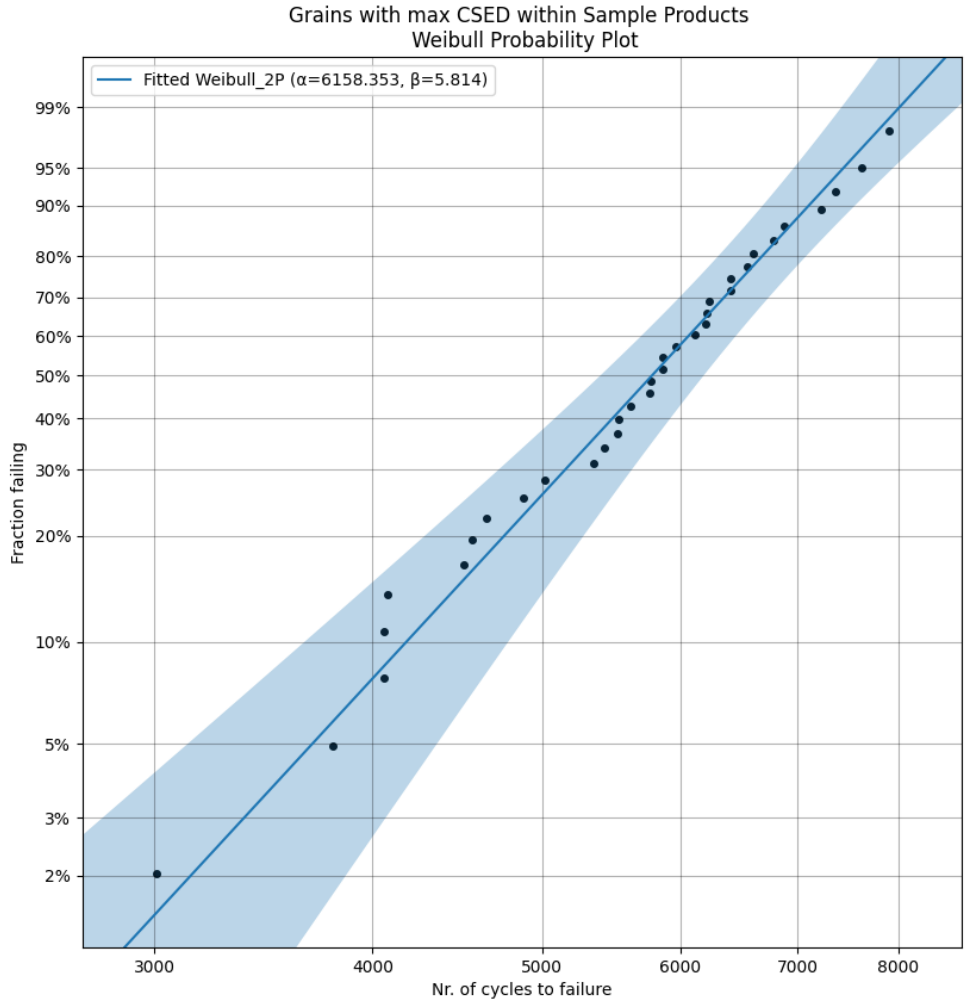

Figure 5.13: Weibull probability plot of grains with maximum CSED in each sample product

The Weibull slope for this dataset is β = 5.81. Internal reliability analyses from NXP and literature on packages with truncated-sphere solder joints (WLCSP and Ball Grid Array) for similar thermal cycling conditions [48] report values of β between $\approx$ 3.4 and $\approx$ 6.7. Figure 5.14 shows two Weibull reliability plots from an internal WLCSP thermal cycling test. The difference in the two legs is the solder joint height: leg 1 features a height of 180 μm and for leg 2 it is

230 μm.

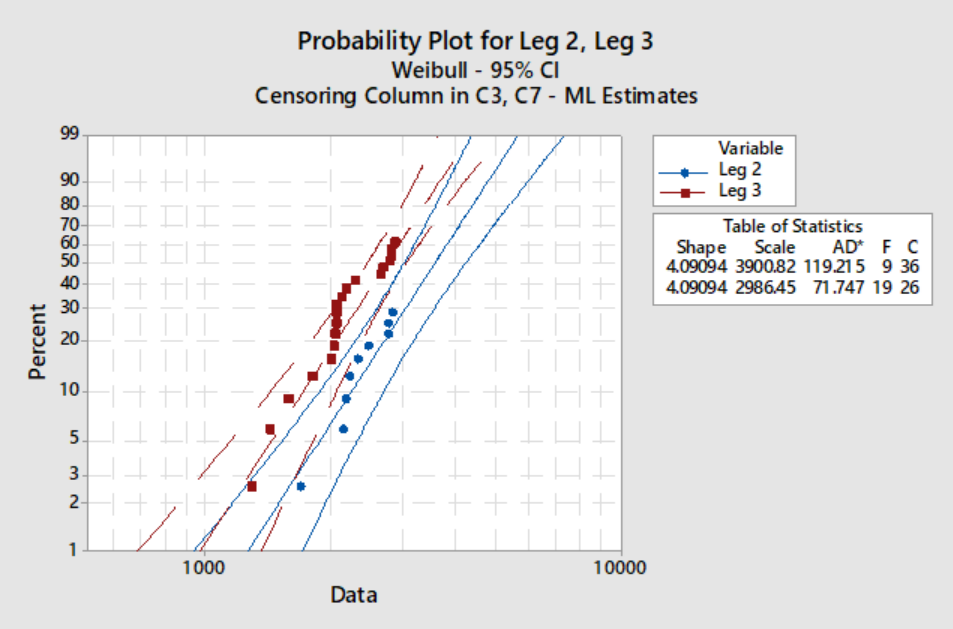

Figure 5.14: Internal reliability data for a WLCSP product

Both legs have the same Weibull slope β = 4.1. It was mentioned earlier in this section that a higher Weibull slope means there is a lower spread in a distribution. Therefore, it is logical that a real-life reliability test results in a lower β than the simulated distribution, since a real-life test has a higher number of factors influencing the possible outcome and thus increasing the spread in results. One last consideration that can be made from the data in Figure 5.13 is the range between the first and last failure: the last failure happens at a number of cycles $\approx$ 2.6 times higher than the first failure.

6

Conclusion & Recommendations

The objective of this thesis was to implement a new microstructure-based FEM technique to simulate the behavior of $SnAgCu$ solder joints and use it to estimate the microstructure-induced variability in solder joint creep response during thermal cycling tests. This method is based on the typical microstructural features of $SnAgCu$ solder joints and combines the Garofalo-Hill anisotropic creep model for the $\beta - Sn$ grains and interface elements fitted with an isotropic creep model for the grain boundaries. Unique grain geometries were obtained for multiple solder joints by means of Voronoi tessellations. The two material constitutive models were implemented in the Marc Mentat finite element software. The script used to generate the Voronoi tessellations was developed in Python and Marc Mentat. The combined implementation of these modeling techniques was validated by replicating a study by Hauck et al. [35], obtaining satisfying results.
The modeling technique was then used in three simulation campaigns to analyze the effect of differences in solder joint structure on large numbers of unique joints as well as on sample WLCSP products fitted with nine solder joints each. The CSED accumulated over the thermal cycles was extracted and used as the main variable of interest, as it is correlated to solder joint fatigue damage.

Analysis on isolated solder joints exposed to the same boundary conditions found that the most creep-sensitive joints accumulated $\approx$ 2.5 times as much CSED than the least sensitive ones. The most critical grain from each solder joint was analyzed, as they would be the most likely sites for fatigue crack initiations. According to this criterion, a maximum lifetime variability of a factor of $\approx$ 4.6 is to be expected for individual solder joints.
The same criterion was also applied on a product level, by considering the most critical grain from each sample product . The distribution of CSED values in the critical grains was then compared with internal reliability data from NXP to find a slightly lower variability than that of real-life tests. The simulated sample products show a difference of a factor of $\approx$ 2.6 between

the first and the last failure according to the ”most critical grain” criterion. The obtained distributions and the modeling technique developed in this project may be used to provide preliminary design margins with respect to solder joint fatigue. In particular, they may yield insight on when the earliest fatigue failures are expected to happen before starting the product test phase.

6.1. Opportunities for Improvement

Although the microstructural modeling technique used in this thesis is more complex than most of the current practices in industry, there is still room for improvement. Some microstructural features such as IMCs were not included in the modeling strategy devised for this project. The impact of IMCs on solder joint fatigue has been researched [24], so including them in the modeling technique might make the simulations more accurate. Other simplifications had to be made for the sake of computational feasibility, such as treating some material properties as constant when in reality they would be temperature-dependent.

The effect of fatigue damage on the solder joint microstructure was also not considered. Literature shows that the $\beta - Sn$ grains recrystallize as fatigue cracks progress through the joint [13] and that these cracks develop along intergranular paths [49]. Interface elements have also been previously used to model fracture at the grain boundaries [50]. The constitutive model used for the interface elements in this thesis could thus be enhanced with a damage variable in order to allow for predictions of intergranular cracking. In addition, localized Voronoi tessellations could be used to re-model the recrystallized grains along the crack front as damage develops in the solder joint.

One drawback of the third simulation campaign is that the solder joint array featured in the sample product is quite small at 3x3. This made it difficult to decouple the effect of the microstructure on the accumulated CSED from that of the solder joint location. Repeating the campaign with a larger solder array should diminish the effect of location between adjacent solder joints and thus allow to better quantify the effect of the microstructural variability. However, this would require considerable computational resources as the FE models for sample products used in this thesis were already quite computationally expensive.

References

[1] L.P.Hunter. *Handbook of Semiconductor Electronics*. McGraw Hill, 1956.

[2] O. Albrecht, H. Wohlrabe, and K. Meier. “Impact of Warpage Effects on Quality and Reliability of Solder Joints”. In: *2019 42nd International Spring Seminar on Electronics Technology (ISSE)* (2019).

[3] P.A. Engel. *Structural Analysis of Printed Circuit Board Systems*. Springer-Verlag, 1993.

[4] S. Su et al. “Fatigue Properties of Lead-free Doped Solder Joints”. In: *2018 17th IEEE Intersociety Conference on Thermal and Thermomechanical Phenomena in Electronic Systems (ITherm)* (2018).

[5] T.R. Bieler et al. “Influence of Sn Grain Size and orientation on the Thermomechanical Response and Reliability of Pb-free Solder Joints”. In: *IEEE Transactions on Components and Packaging Technologies, vol. 31, no. 2, pp. 370-379* (2008).

[6] L.P. Lehman et al. “Microstructure and Damage Evolution in Sn-Ag-Cu Solder Joints”. In: *Electronic Components and Technology (ECTC)* (2005).

[7] D. Mondal et al. “Modeling Deformation Behavior of Multiple Grained SAC305 Solder Joints”. In: *2020 19th IEEE Intersociety Conference on Thermal and Thermomechanical Phenomena in Electronic Systems (ITherm), pp. 1221-1228* (2020).

[8] J. Gleichauf, Y. Maniar, and S. Wiese. “Reliability testing of solder joints under combined cyclic thermal and bending load for automotive applications”. In: *Microelectronics Reliability, vol.139, pp.114791* (2022).

[9] D.Y.R. Chong et al. “Drop Impact Reliability Testing for Lead-Free and Leaded Soldered IC Packages”. In: *Electronic Components and Technology Conference* (2005).

[10] H. Ye et al. “Reliability evaluation of CSP soldered joints based on FEM and Taguchi method”. In: *Computational Materials Science* (2010).

[11] A. Syed. “Accumulated creep strain and energy density based thermal fatigue life prediction models for SnAgCu solder joints”. In: *Proc. 54th Electron. Comp. Technol. Conf. vol. 125, pp.737-746* (2004).

[12] K.N. Subramanian and J.G. Lee. “Effect of anisotropy of tin on thermomechanical behavior of solder joints”. In: *J. Mater. Sci.: mater. Electron., vol. 15, pp. 235-240* (2004).

[13] D.W. Henderson et al. “The microstructure of Sn in near-eutectic Sn–Ag–Cu alloy solder joints and its role in thermomechanical fatigue”. In: *J.Mater.Res., vol.19, no.6, pp.1608-1612* (2004).

[14] A.U. Telang et al. “Grain Boundary Character and Grain Growth in Bulk Tin and Bulk Pb-free Solder Alloys”. In: *Journal of Electronic Materials, vol.33, pp.1412-23* (2004).

[15] S. Lia et al. “Microstructure and hardness of SAC305 and SAC305-0.3Ni solder on Cu, high temperature treated Cu, and graphene-coated Cu substrates”. In: *Result in Physics, vol.11, pp.617-622* (2018).

[16] Q. Jiang, A.N. Deshpande, and A. Dasgupta. “Grain-Scale Anisotropic Analysis of Steady-State Creep in Oligocrystalline SAC Solder Joints”. In: *Materials, vol.14, pp.5973* (2021).

[17] M.H. Mahdavifard et al. “The effect of iron and bismuth addition on the microstructural, mechanical, and thermal properties of Sn–1Ag–0.5 Cu solder alloy”. In: *Microelectron. Reliab. vol.55, pp.1886-1890* (2015).

[18] M. Ering, P.J.G. Schreurs, and M.G.D. Geers. “Intergranular thermal fatigue damage evolution in SnAgCu lead-free solder”. In: *Mech. Mater., vol.40, pp.780-791* (2008).

[19] M.A. Matin, W.P. Vellinga, and M.G.D. Geers. “Aspects of coarsening in eutectic Sn-Pb”. In: *Acta Mater., vol.52, pp.3475-3482* (2004).

[20] K.N. Subramanian. “Role of anisotropic behaviour of Sn on thermomechanical fatigue and fracture of Sn-based solder joints under thermal excursions”. In: *Fatigue Fract. Eng. Mater. Struct., vol.30, pp.420-431* (2007).

[21] A. Deshpande et al. “Impact of interfacial roughness on tensile vs. shear creep rupture of solder joints”. In: *20th IEEE Intersociety Conference on Thermal and Thermomechanical Phenomena in Electronic Systems (iTherm)* (2021).

[22] O. Krammer. “Comparing the reliability and intermetallic layer of solder joints prepared with infrared and vapour phase soldering”. In: *Soldering and Surface Mount Technology, vol.26, pp.214-222* (2014).

[23] R. Darveaux et al. “Effect of Joint Size and Pad Metallization on Solder Mechanical Properties”. In: *Electronic Components and Technology Conference* (2008).

[24] W. Sun et al. “Study of Five Substrate Pad Finishes for the Co-design of Solder Joint Reliability under Board-level Drop and Temperature Cycling Test Conditions”. In: *International Conference on Electronic Packaging Technology & High Density Packaging (ICEPT-HDP)* (2008).

[25] Q. Jiang, A. Deshpande, and A. Dasgupta. “Multi-scale Crystal Viscoplasticity Approach for Estimating Anisotropic Steady-State Creep Properties of Single-Crystal SnAgCu Alloys”. In: *International Journal of Plasticity, vol. 153* (2022).

[26] F.W. Crossman and M.F. Ashby. “The non-uniform flow of polycrystals by grain- boundary sliding accommodated by power-law creep”. In: *Acta Metallurgica, vol.23, pp.425-440* (1975).

[27] Q. Jiang and A. Dasgupta. “Anisotropic Multi-scale Modeling For Steady-State Creep Behavior of Oligocrystalline SnAgCu (SAC) Solder Joints”. In: *University of Maryland, Department of Mechanical Engineering* (2021).

[28] M.Motalab and P.Lall. “Determination of Anand constants for SAC solders using stress-strain or creep data”. In: *Thermal and Thermomechanical Phenomena in Electronic Systems (ITherm), 2012 13th IEEE Intersociety Conference* (2012).

[29] E.H. Amalu and N.N. Ekere. “Modelling evaluation of Garofalo-Arrhenius creep relation for lead-free solder joints in surface mount electronic component assemblies”. In: *Journal of Manufacturing Systems* (2016).

[30] A. Schubert et al. “Fatigue life models for SnAgCu and SnPb solder joints evaluated by experiments and simulation.” In: *Electronic Components and Technology Conference* (2003).

[31] J. Catellanos et al. “Analysis of Garofalo equation parameters for an ultrahigh carbon steel”. In: *Journal of Materials Science volume 45, pages5522–5527* (2010).

[32] R. Hill. *The Mathematical Theory of Plasticity*. Oxford Classic Texts in the Physical Sciences, 1950.

[33] M. Serebreni, R. Wilcoxon, and F.P. McCluskey. “Modeling the Influence of Conformal Coatings on Thermo-Mechanical Fatigue of Solder Interconnects in Electronic Packages”. In: *HiTEC Conference at Albuquerque, New Mexico* (2018).

[34] M. van Soestbergen and J.J.M. Zaal. “Predictive modeling of competing failure mechanisms using a dedicated constitutive relation for solder alloy”. In: *IEEE* (2018).

[35] T. Hauck et al. “Virtual Testing and Digital Twin Approaches for Response of Grain-scale Solder Interconnects to Multiaxial Loading”. In: *2022 23rd International Conference on Thermal, Mechanical and Multi-Physics Simulation and Experiments in Microelectronics and Microsystems (EuroSimE)* (2022).

[36] G. Sfantos and M. Aliabadi. “A boundary cohesive grain element formulation for modelling intergranular microfracture in polycrystalline brittle materials”. In: *international Journal for Numerical Methods in Engineering, vol.69, pp.1590-1626* (2007).

[37] T. Luther and C. Könke. “Polycristal models for the analysis of intergranular crack growth in metallic materials”. In: *Eng. Fract. Mech., vol.76, pp.2332-2343* (2009).

[38] J.R. Spingarn and W.D. Nix. “A model for creep based on the climb of dislocations at grain boundaries”. In: *Acta Metallurgica, vol.27, pp.171-177* (1979).

[39] T. An and F. Qin. “Intergranular Cracking Simulation of the Intermetallic Compound Layer in Solder Joints”. In: *Computational Materials Science, vol.79, pp. 1-14* (2013).

[40] Arkadiusz Żydek, Mariusz Wermiński, and Marcela E. Trybula. “Description of grain boundary structure and topology in nanocrystalline aluminum using Voronoi analysis and order parameter”. In: *Computational Materials Science, vol.197, pp.110660* (2021).

[41] J. Wu and R. Lee. “The advantages of triangular and tetrahedral edge elements for electromagnetic modeling with the finite-element method”. In: *IEEE Transactions on Antennas and Propagation, vol.45 no.9, pp.1431-1437Ft* (1997).

[42] R. Cruz and V. Gonda. “Solder joint reliability based on creep strain energy density for SAC305 and doped SAC solders”. In: *MATEC Web of Conferences, vol.343, pp. 02005* (2021).

[43] R. Jiang and D.N.P. Murthy. “A study of Weibull shape parameter: Properties and significance”. In: *Reliability Engineering & System Safety, vol.96, nr.12, pp.1619-1626* (2011).

[44] W. Nelson. *Applied Life Data Analysis*. Addison-Wesley, 1982.

[45] M. van Soestbergen et al. “Reduction of empiricism in the solder joint reliability assessment of QFN packages by using thermo-mechanical simulations”. In: *2023 24th International Conference on Thermal, Mechanical and Multi-Physics Simulation and Experiments in Microelectronics and Microsystems (EuroSimE)* (2023).

[46] Y. Chen et al. “Analysis of the BGA solder Sn–3.0Ag–0.5Cu crack interface and a prediction of the fatigue life under tensile stress”. In: *International Journal of Fatigue, vol.87, pp.216-224* (2016).

[47] Renesas Electronics. “Wafer-level Chip Scale Package (WLCSP) Implementation Guidelines”. In: *application note* (2023).

[48] J.H. Lau et al. “Thermal Cycling Test and Simulation of Six-Side Molded Panel-Level Chip-Scale Packages (PLCSPs)”. In: *Microelectronics and Electronic Packaging, vol.18, pp.67-80* (2021).

[49] E. Ben Romdhane and P. Roumanille et al. “From early microstructural evolution to intergranular crack propagation in SAC solders under thermomechanical fatigue”. In: *Institut de Recherche Technologique Saint-Exupéry, Toulouse, France & IMS Laboratory, University of Bordeaux, Talence, France & Elemca, Toulouse, France* (year not mentioned).

[50] V.N Le et al. “Modeling of intergranular thermal fatigue cracking of a lead-free solder joint in a power electronic module”. In: *International Journal of Solids and Structures, vol.106-107, pp.1-12* (2017).

A

Implicit Garofalo-Hill Formulation

The implicit Garofalo-Hill formulation has been implemented in Marc by means of a subroutine, in a similar way to the grain boundary constitutive model. The UVSCPL subroutine allows the user to define their own elastic-viscoplastic constitutive model.

List of assumptions

The following assumptions have been used while developing this implementation:

1. The relationship between the stress rate and the elastic strain rate is given by Hooke's law;
2. The contribution of plasticity to inelastic behavior is negligible compared to the contribution from creep [33];
3. The relationship between strain rate and stress is linear within the time increment.

According to Marc documentation, the required outputs for subroutine UVSCPL are the inelastic strain increment and the stress increment. The derivation to obtain both starts from Hooke's law applied to stress and strain *rates* rather than stress and strain:

$$\dot{\sigma} = \mathbf{D}(\dot{\epsilon}^{el}) \tag{A.1}$$

where **D** is the elastic stiffness matrix and $\dot{\epsilon_{el}}$ is the elastic strain rate. The total strain rate is then split up according to the Maxwell material representation, in which the strain rate is considered the sum of its elastic, plastic and creep components, see Figure 2.6. However, one of the listed assumptions mentions that the contribution of plastic strain to the total strain is negligible in this case. This leads to:

$$\dot{\epsilon_{tot}} = \dot{\epsilon}^{el} + \dot{\epsilon}^{cr} \tag{A.2}$$

now, Equation A.1 can be rewritten as:

$$\dot{\sigma} = \mathbf{D}(\dot{\epsilon}^{tot} - \dot{\epsilon}^{cr}) \tag{A.3}$$

In Equation 2.4 the equivalent creep strain rate $\dot{\bar{\epsilon}}_{cr}$ was defined as a function of the Hill equivalent stress, here listed as $\bar{\sigma}$. The gradient to the Hill stress was then used in Equation 2.5 to obtain the creep strain rate tensor:

$$\dot{\epsilon}_{ij}^{cr} = \frac{\partial \bar{\sigma}}{\partial \sigma_{ij}} \dot{\bar{\epsilon}}^{cr} \tag{A.4}$$

A Taylor series expansion is then applied to the expression for the equivalent creep strain rate:

$$\dot{\epsilon}_{ij}^{cr} = \frac{\partial \bar{\sigma}}{\partial \sigma_{ij}} (\dot{\bar{\epsilon}}^{cr_0} + \frac{\partial \dot{\bar{\epsilon}}^{cr}}{\partial \bar{\sigma}} (\frac{\partial \bar{\sigma}}{\partial \sigma_{ij}})^T \Delta\sigma_{ij}) \tag{A.5}$$

By assumption, the dependency between creep strain rate and the stress is linear within the time increment Δt. This allows to integrate the creep strain rate over Δt and obtain the creep strain increment $\Delta\epsilon_{ij}^{cr}$:

$$\Delta\epsilon_{ij}^{cr} = \frac{\partial \bar{\sigma}}{\partial \sigma_{ij}} \dot{\bar{\epsilon}}^{cr_0} \Delta t + \frac{\partial \bar{\sigma}}{\partial \sigma_{ij}} \alpha (\frac{\partial \bar{\sigma}}{\partial \sigma_{ij}})^T \Delta\sigma \qquad with \qquad \alpha = \frac{1}{2} \frac{\partial \dot{\bar{\epsilon}}^{cr}}{\partial \bar{\sigma}} \Delta t \tag{A.6}$$

The stress increment $\Delta\sigma$ in Equation A.6 can be expressed as a function of the strain increment via Hooke's law;

$$\Delta\sigma_{ij} = \mathbf{D}(\Delta\epsilon_{ij} - \Delta\epsilon_{ij}^{cr}) \tag{A.7}$$

Based on Equation A.7, it is possible to solve for $\Delta\sigma_{ij}$ by using Equation A.6 and the Sherman-Morrison formula:

$$(\mathbf{A} + uv^T)^{-1} = \mathbf{A}^{-1} - \frac{\mathbf{A}^{-1} u v^T \mathbf{A}^{-1}}{1 + v^T \mathbf{A}^{-1} u} \tag{A.8}$$

in which $\mathbf{A}$ is a square matrix and u, v are vectors. The final result for the stress increment then is:

$$\Delta\sigma_{ij} = (\mathbf{D} - (1-p) \frac{\mathbf{D} \frac{\partial \bar{\sigma}}{\partial \sigma_{ij}} (\frac{\partial \bar{\sigma}}{\partial \sigma_{ij}})^T \mathbf{D}}{(\frac{\partial \bar{\sigma}}{\partial \sigma_{ij}})^T \mathbf{D} \frac{\partial \bar{\sigma}}{\partial \sigma_{ij}}}) (\Delta\epsilon_{ij} - \dot{\epsilon}_0^{cr} \Delta t) \quad with \quad p = \frac{1}{1 + \frac{1}{2} \frac{\partial \dot{\bar{\epsilon}}^{cr}}{\partial \bar{\sigma}} \Delta t \frac{\partial \bar{\sigma}}{\partial \sigma_{ij}} \mathbf{D} \frac{\partial \bar{\sigma}}{\partial \sigma_{ij}}} \tag{A.9}$$

B

Project Plan

The planning for this thesis project was done in concurrence with the literature study in preparation for the project. The literature review performed before the beginning of the project is not included. The theoretical knowledge used in this project was presented in chapter 2.

The first part of the project consisted of redefining the project plan and getting acquainted with additional literature to support the updated plan. Most of the literature researched in this phase was about the Garofalo-Hill anisotropic creep model and grain boundary modeling techniques.

Once the background knowledge was sufficiently solid, the different software used for the FE simulations had to be learned. Skills for the FE software Marc Mentat skills were revised and Fortran basics were learned. At this point all the necessary knowledge needed to implement the custom constitutive models in Marc Mentat had been obtained. The last two months before the midterm meeting were dedicated to developing and validating the Fortran subroutines for the Garofalo-Hill equations and the grain boundary constitutive model.

The project resumed after the Christmas break with a validation study of the combined Garofalo-Hill and grain boundary constitutive models. Then the next big task of the project took place, in which the Python code to generate randomized solder joint microstructures was developed and implemented in Marc Mentat. At this point in the project the Finite Element models for the single solder joints were ready and, once convergence studies were performed, the simulation campaigns could start.

The last phase of the project consisted of creating a Python script to generate the Finite Element models of the sample products and subsequently use them for the last simulations.

Concurrently, statistical analysis was performed on all the simulation results obtained.
An overview of the project plan is given in the form of a Gantt chart in Figure B.1

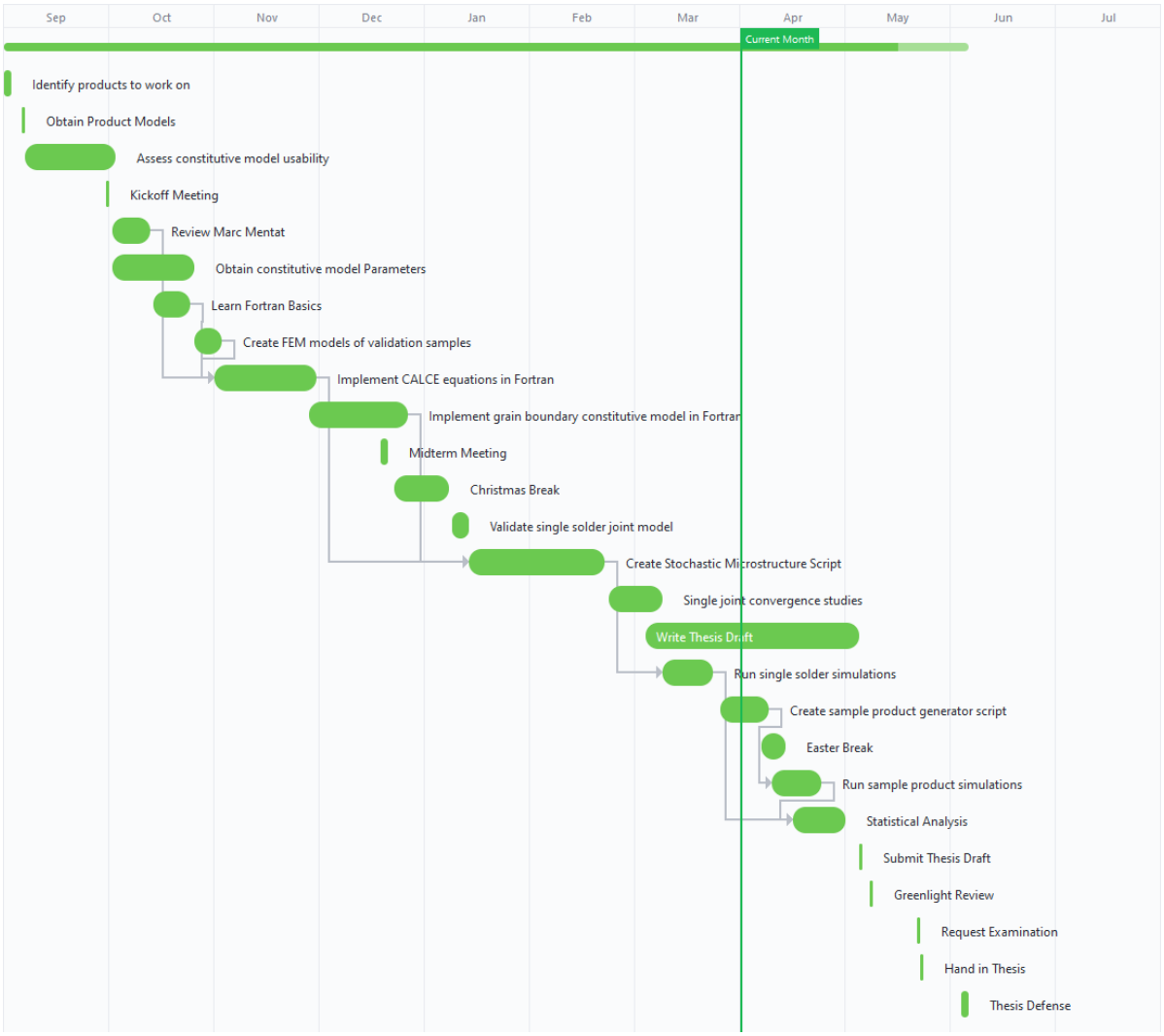

Figure B.1: Gantt Chart of the thesis project plsn